LITHOS 514–515 (2025) 108211

Contents lists available at ScienceDirect

LITHOS

journal homepage: www.elsevier.com/locate/lithos

Sub-solidus evolution of plagioclase-hosted Fe-Ti oxide micro-inclusions from oceanic gabbros, Mid-Atlantic ridge (10–13°N)

Ge Bian [a,*], Olga Ageeva [a,b], Alexey Pertsev [b], Andras Kovacs [c], Gerlinde Habler [a], Qianqian Lan [c], Rafal E. Dunin-Borkowski [c], Olga Zhilicheva [b], Rainer Abart [a]

[a] Department of Lithospheric Research, University of Vienna, Josef-Holaubek-Platz 2, 1090 Vienna, Austria
[b] Institute of Geology of Ore Deposits, Petrography, Mineralogy and Geochemistry of the Russian Academy of Sciences (IGEM RAS), Staromonetnyi 35, Moscow 119017, Russia
[c] Ernst Ruska-Center for Microscopy and Spectroscopy with Electrons (ER-C), Forschungzentrum Jülich GmbH, Wilhelm-Johnen-Strasse, 52428 Jülich, Germany

ARTICLE INFO

Keywords:
Fe—Ti oxide micro-inclusions
Plagioclase host
Sub-solidus evolution
Oceanic gabbro
Remanent magnetization

ABSTRACT

Iron-titanium oxide minerals are highly reactive under changing *P-T-f*O_2 conditions, and their chemical compositions and phase relations are important petrogenetic indicators. In this study, we use optical-, scanning electron-, and scanning transmission electron microscopy to investigate the sub-solidus and hydrothermal evolution of plagioclase-hosted Fe—Ti oxide micro-inclusions from two types of oceanic gabbro dredged from the Mid-Atlantic Ridge at 10–13°N and exhibiting different types of hydrothermal alterations. Initially, the micro-inclusions formed as oriented, needle-shaped titanomagnetite, by precipitation from Fe- and Ti-bearing plagioclase. In most of the studied gabbros, such inclusions evolved into magnetite-ilmenite intergrowths by high-temperature oxidation above the Curie temperature of magnetite. Further evolution of the Fe—Ti oxide micro-inclusions occurred during hydrothermal alteration at temperatures below the Curie temperature. Under low-intensity hydrothermal alteration, the micro-inclusions underwent minor dissolution and recrystallization. In contrast, intensive hydrothermal alteration under relatively reducing conditions resulted in substantial recrystallization and formation of magnetite-ulvospinel micro-inclusions, which were subsequently transformed into fine-grained magnetite-ilmenite ± ulvospinel aggregates. The phase contents and the microstructures of the plagioclase-hosted Fe—Ti oxide micro-inclusions, formed during the sub-solidus and hydrothermal evolution, provide insights into their evolution during cooling under changing redox conditions. These features are crucial for interpreting paleomagnetic measurements of Fe-rich gabbros, which often feature plagioclase hosting Fe—Ti oxide micro-inclusions.

1. Introduction

Magnetic minerals in rocks can capture and retain the Earth's magnetic field over geological times, a phenomenon that is known as natural remanent magnetization (NRM). Among various forms of NRM, thermal remanent magnetization (TRM) is crucial for paleomagnetic studies. At high temperatures, most magnetic minerals are dia- or paramagnetic and, when they cool through their Curie temperature (T_c), they attain a ferromagnetic state, where their magnetization is aligned with the Earth's magnetic field. Upon further cooling, this alignment becomes fixed, resulting in TRM, which remains stable over long periods, making it a reliable indicator for paleomagnetic reconstructions (Dunlop and Özdemir, 1997). Fe—Ti oxides are the most important magnetic minerals in rocks (Ferré et al., 2021). They may occur as individual grains or as micro-inclusions in rock-forming silicates, thereby imparting ferromagnetism to otherwise para- or diamagnetic silicate host crystals. The magnetic properties of silicates containing Fe—Ti oxide micro-inclusions depend on the spatial distribution, shape as well as shape- and crystallographic orientation of the Fe—Ti oxide micro-inclusions relative to their silicate host.

Oriented Fe—Ti oxide micro-inclusions have frequently been observed in rock-forming silicates from mafic plutonic and metamorphic

* Corresponding author at: Fort Hoofddijk, Faculty of Geosciences, Utrecht University, Budapestlaan 17, 3584 CD Utrecht, the Netherlands.
E-mail addresses: biang92@univie.ac.at, g.bian@uu.nl (G. Bian), olga.ageeva@univie.ac.at (O. Ageeva), pertsev2igem@gmail.com (A. Pertsev), a.kovacs@fz-juelich.de (A. Kovacs), gerlinde.habler@univie.ac.at (G. Habler), q.lan@fz-juelich.de (Q. Lan), r.dunin-borkowski@fz-juelich.de (R.E. Dunin-Borkowski), ozhilich@igem.ru (O. Zhilicheva), rainer.abart@univie.ac.at (R. Abart).

https://doi.org/10.1016/j.lithos.2025.108211
Received 13 November 2024; Received in revised form 26 June 2025; Accepted 28 July 2025

rocks. Examples include olivine (Champness, 1970; Knafelc et al., 2019), pyroxene (Ageeva et al., 2017; Gao et al., 2019; Hwang et al., 2010; Nikolaisen et al., 2022; Renne et al., 2002; Zhao et al., 2022) and plagioclase (Ageeva et al., 2016; Hwang et al., 2024; Kato et al., 2024; Sobolev, 1990; Wenk et al., 2011). The Fe—Ti oxide micro-inclusions may be single-phase, or they may be comprised of an intergrowth of several different Fe—Ti oxide minerals, including magnetite ($Fe^{2+}Fe_2^{3+}O_4$), ilmenite ($Fe^{2+}TiO_3$), ulvospinel ($Fe_2^{2+}TiO_4$) and hematite ($Fe_2^{3+}O_3$). The micro-inclusions often occur as several hundred nanometers wide and hundreds of micrometers long needles and laths with systematic crystallographic and shape orientation relationships (CORs and SORs) to their silicate host. Due to their small size and high aspect ratio (length-to-width ratio), such Fe—Ti oxide micro-inclusions behave as single-domain or pseudo-single-domain magnetic particles (Dunlop and Özdemir, 1997), which show a high coercivity and thus are very resistant to changes of the external magnetic field. They are also well protected from external physical and chemical influences by the silicate host and, therefore, are particularly robust recorders of paleomagnetic signals.

In this study, we focus on the sub-solidus and hydrothermal evolution of plagioclase-hosted Fe—Ti oxide micro-inclusions from oceanic gabbro dredged at the Mid-Atlantic ridge at 10–13°N, 45–47°W. These inclusions mostly display needle or lath shape and usually comprise different Fe—Ti oxide phases including magnetite as the majority phase, as well as ilmenite and ulvospinel as additional phases, often forming oriented intergrowth with the magnetite. Based on the SORs and CORs between the magnetite (mag) inclusions and plagioclase (PL) host,[1] two inclusion types have been discerned in plagioclase from oceanic gabbro: (i) plane-normal-type and (ii) pl[001]-type inclusions (Ageeva et al., 2020). Needle-shaped plane-normal-type micro-inclusions are elongated parallel to one of the mag⟨111⟩ directions, which, in turn, is parallel to one of seven specific crystallographic directions in plagioclase, including pl(112)n, pl($\bar{3}$12)n, pl(1$\bar{5}$0)n, pl(150)n, pl(100)n, pl(1$\bar{1}$2)n and pl($\bar{3}$1$\bar{2}$)n, where pl(*hkl*)n indicates the normal direction to the (*hkl*) lattice plane of plagioclase. The plane-normal-type inclusions were inferred to have precipitated from Fe- and Ti-bearing plagioclase in a solid-state reaction or in a sequence of solid-state reactions at temperatures above about 600 °C (Bian et al., 2021). The Fe—Ti oxide micro-inclusions of the pl[001]-type have their elongation directions parallel to one of the mag⟨110⟩ directions, which is, in turn, aligned parallel to the pl[001] direction. The majority of pl[001]-type inclusions were formed by recrystallization of preexisting plane-normal-type inclusions during high-temperature (HT) hydrothermal alteration (Ageeva et al., 2022; Bian et al., 2023a). A small fraction of pl[001]-type inclusions, as shown below, may have formed through precipitation from Fe- and Ti-bearing plagioclase simultaneously with the plane-normal-type inclusions.

Although largely shielded from external influence by their silicate host, the plagioclase-hosted Fe—Ti oxide micro-inclusions undergo a sequence of transformations in response to changes in the physico-chemical conditions during their sub-solidus evolution. As a consequence, even if the primary NRM of these micro-inclusions may have been acquired at temperatures above the T_C of magnetite and thus needs to be considered as TRM, their magnetization may have been changed due to the transformations they underwent during their sub-solidus evolution and may have become chemical remanence magnetization (CRM) (Feinberg et al., 2006). In this study, the evolution of the phase compositions and internal microstructures of plagioclase-hosted Fe—Ti oxide micro-inclusions of two types of oceanic gabbro with different petrogenetic histories is addressed. This includes an analysis of morphological and compositional variations, as well as a microstructural and textural analysis of the Fe—Ti oxide micro-inclusions using several microanalytical techniques, including optical-, scanning electron-, and scanning transmission electron microscopy. Distinct sequences of mineral reactions and internal microstructures are inferred for the plagioclase-hosted Fe—Ti oxide micro-inclusions in the two different types of gabbro with implications for their NRM behavior.

[1] Abbreviation of mineral names are after IMA-CNMNC (2020). We use lowercase letters for inclusion phases and uppercase letters for the silicate host phases.

2. Material and methods

2.1. Material

For this study, we used samples of oceanic gabbro from two geological settings at the Mid-Atlantic ridge, which were collected during the 26th (2005) and 30th (2007) cruises of the r/v "Professor Logachev" (Polar Marine Geosurvey Expedition). The samples pertain to two different rock types, which have different petrogenetic histories as reflected by their mineralogical compositions. The samples are henceforth referred to as *non-altered gabbro* and *altered gabbro*. The sample characteristics are summarized in Table 1.

Non-altered gabbro (Samples L30–277-7, L30–277-10, 1491–10, 1514–17) was dredged from the Ashadze oceanic core complex (OCC), which is actively developing in the footwall of a large offset extensional detachment fault at the western flank of the Mid-Atlantic ridge rift valley at 13°N 45°W (Peirce et al., 2020, 2019). The Ashadze OCC is mainly comprised of mantle peridotite (Pertsev et al., 2009; Sholukhov et al., 2022), which hosts black smoker vent fields (Ashadze-1 and -2) (Ondréas et al., 2012). The samples are medium-grained gabbro with Fe—Ti oxides <5 vol% (Sample L30–277-7, L30–277-10), and medium-grained oxide gabbro (1491–10 and 1514–17), that is gabbro with >5 vol% Fe—Ti oxide minerals. The oxide gabbro contains relics of coarse-grained gabbronorite. All samples comprise plagioclase (~ 50 vol%), clino- and orthopyroxene, amphibole, and Fe—Ti oxides. Clinopyroxene and rarely orthopyroxene occur as subhedral 3–5 mm-sized grains, which were partially replaced by magnesiohornblende during weak HT hydrothermal alteration. The Fe—Ti oxides are represented by up to about 1 mm-sized grains of ilmenite, magnetite, and ilmenite-magnetite intergrowth. These grains typically occupy interstitial positions between the rock-forming silicate minerals. The content of Fe—Ti oxides varies from <0.5 vol% (Sample L30–277-7, L30–277-10) up to about 5 vol% (Sample 1491–10, 1514–17). In addition, Fe—Ti oxides are present as oriented needle and lath-shaped micro-inclusions in plagioclase and pyroxene (Ageeva et al., 2016; Ageeva et al., 2020; Bian et al., 2021; Bian et al., 2023a, 2023b).

Table 1
Sampling sites and rock characteristics.

Location	*Non-altered gabbro*: (core) complex Ashadze			*Altered* gabbro: VLS
Sample	L30–277-7/-10	1491–10	1514–17	L2612–41
Dredge station	Dredge L30–277	Dredge 1491	TV-grab 1514	L2612
Latitude1	13.02715 N	12.98967 N	12.98873 N	10.708
Latitude2	13.03357 N	12.99057 N		10.693
Longitude1	44.86868 W	44.90620 W	44.86057 W	41.570 W
Longitude2	44.87205 W	44.91003 W		41.583 W
Depth1 (mbsl*)	4089	3300	4116	5195
Depth2 (mbsl)	3922	3280		4620
Characteristics	Medium-grained gabbro. Fe—Ti oxides <5 %	Medium-grained oxide gabbro	Medium-grained oxide gabbro with coarse-grained gabbronorite relics	Medium-grained oxide gabbro

* msbl: meter below sea level.

Altered gabbro (Sample L2612–41) was collected from the Vema Lithospheric Section (VLS) at 10°42′ N 41°35′ W and was studied in detail by Pertsev et al. (2015). The VLS is exposed at the uplifted southern wall of the Vema Transform Fault. The VLS consists of serpentinized mantle peridotite, gabbro, dolerite dykes and basaltic lavas (Auzende et al., 1989; Bonatti et al., 2003; Bonatti et al., 2005; Cipriani et al., 2009) and is located near the ridge-transform intersection, an area which is characterized by intensive fracturing and hydrothermal alteration of the thin magmatic crust and the underlying mantle (Hooft et al., 2000; Wolfe et al., 1995). The lower crustal rocks of the VLS are dominated by oxide gabbro, whereas primitive olivine-bearing rocks are rare. Brunelli et al. (2020) and Pertsev et al. (2015) reconstructed the magmatic and hydrothermal history of a VLS oxide gabbro, which had been dredged together with serpentinized mantle peridotites. In particular, these latter authors addressed features of sample L2612–41, which are indicative of a HT hydrothermal processing that was ascribed to the ingress of high-salinity reducing fluid at temperatures of up to about 600 °C (Pertsev et al., 2015). The mineralogical composition and the microstructures in *altered gabbro* reflect three evolutionary stages (Pertsev et al., 2015):

Stage 1 is represented by primary coarse-grained plagioclase (PL_1), clino- and minor orthopyroxene (CPX_1, OPX_1) and corresponds to the early magmatic evolution. The shape of initial prismatic pyroxenes and tabular plagioclase is rarely preserved owing to later deformation and partial mineral replacement.

Stage 2 is associated with the late magmatic evolution and is manifest from intracrystalline deformation of clinopyroxene and plagioclase, formation of mylonitic clinopyroxene (CPX_{2a}) and plagioclase (PL_{2a}), formation of post-deformation interstitial Fe—Ti oxides, and local replacement of CPX_1 by clinopyroxene (CPX_{2b}) – hornblende (HBL_2) ± apatite, and local precipitation of PL_{2b}.

Stage 3 corresponds to HT hydrothermal alteration leading to the filling of cracks in PL_1 by HBL_3 mantled by PL_3, formation of zoned hornblende (HBL_2) along PL_1-CPX_1 contacts and local formation of $HBL_3 + CPX_3$ aggregates.

In the current work, we use the same gabbro sample (Sample Gabbro-41 in Pertsev et al. (2015)) and revise the earlier established plagioclase generations in the light of the presence/absence and character of Fe—Ti oxide micro-inclusions. Geochemical data of the gabbro samples are presented in the Supplementary Material (SM) Table 1.

2.2. Methods

2.2.1. Cathodo-luminescence

Cathodo-luminescence (CL) images in actual colors were taken with a "Cameca" MS-46 electron microprobe equipped with an optical system and a high-resolution digital camera "Videoscan-285" and Videoscan Viewer software (Institute of Geology of Ore Deposits, Petrography, Mineralogy, and Geochemistry of Russian Academy of Sciences, Moscow). The CL was activated by an electron beam using an acceleration voltage of 20 kV and a beam current of 40 nA on a carbon-coated sample. The CL was captured in a 300 × 300 μm raster using an exposure time of 240 s.

2.2.2. Scanning electron microscopy and focused ion beam technique

Secondary electron (SE) imaging and crystallographic orientation analyses using the electron backscatter diffraction (EBSD) technique were carried out using an FEI Quanta 3D FEG-SEM at the FIB-FESEM laboratory of the Core Facility Electron Beam Microanalysis, Faculty of Earth Sciences, Geography and Astronomy at the University of Vienna (AT). The instrument is equipped with a Schottky-type field-emission electron gun and an EDAX Pegasus Apex 4 system and an EDAX Digiview V EBSD camera for crystallographic orientation analysis. SE imaging and EBSD analyses were conducted on chemo-mechanically polished carbon-coated thin sections to identify representative Fe—Ti oxide micro-inclusions for further scanning transmission electron microscopy (STEM) studies. EBSD measurements were performed with an electron beam set to an accelerating voltage of 15 kV and a probe current of approximately 4 nA in analytic mode. The working distance was in the range of 14–14.5 mm, while the thin section surface plane was at 20° tilt with respect to the incident electron beam. Over 1000 micro-inclusions were analyzed using EBSD.

Electron-transparent foils of Fe—Ti oxide micro-inclusions were selectively extracted from the plagioclase host using the focused ion beam (FIB) device on the same FEI Quanta 3D FEG instrument. The ion column of this instrument features a liquid Ga-ion source, a gas injection system for Pt and C deposition, and an Omniprobe 100.7 micromanipulator for in situ lift-out. Combining optical microscopy and EBSD crystal orientation data, five site- and orientation-specific TEM specimens were extracted from the chemomechanically polished carbon-coated thin sections. The progress of FIB milling was monitored by SE imaging with the electron beam set to 15 kV acceleration voltage and approximately 53 pA probe current. FIB-induced SE imaging utilized a 30 kV acceleration voltage and 10 pA probe current. For foil extraction by FIB, 30 kV acceleration voltage was employed with successively decreasing FIB probe currents of 65, 30, 5, and 1 nA. After transfer to a Cu-grid, the foils were thinned to about 100 nm thickness using FIB probe currents successively decreasing from 1 nA to 10 pA. The resulting TEM specimens have dimensions of approximately 20 × 15 μm and are about 100 nm thick. Final cleaning of the foil was prepared using ion beam settings of 5 kV / 48 pA and 2 kV / 27 pA. The following reference structures were used for EBSD indexing of ilmenite (trigonal, Laue group -3; $a = b = 5.09$ Å, $c = 14.09$ Å, $\alpha = \beta = 90°$, $\gamma = 120°$), and of ulvospinel/magnetite (cubic, Laue group $m3m$; $a = b = c = 8.396$ Å, $\alpha = \beta = \gamma = 90°$). The investigated samples and the individual magnetite micro-inclusions extracted from the thin sections are listed in Table 2.

2.2.3. Scanning transmission electron microscopy

The grain internal microstructures, phase contents, and chemical compositions of the micro-inclusions were investigated using site- and orientation-specific FIB foils. These investigations employed High-Angle Annular Dark-Field (HAADF) STEM imaging and Energy Dispersive X-ray (EDX) spectroscopy. STEM analyses were performed at the Ernst Ruska-Center for Microscopy and Spectroscopy with Electrons, Forschungszentrum Jülich, Germany, utilizing a Thermo Fisher 80–200 probe-corrected Titan ChemiSTEM equipped with a four-quadrant Super-X EDX detector. The microscope was operated at an accelerating voltage of 200 kV with a probe convergence angle of 21 mrad. Single HAADF-STEM images and image stacks were acquired using the Velox software, employing drift-corrected frame imaging mode to automatically correct drift in HAADF-STEM images. EDX maps were recorded with the Velox software using a 512 × 512 frame size and a live time of 10 μs per pixel per frame. Drift compensation was applied by accumulating multiple fast frames. Quantitative EDX line profiles were extracted from the EDX maps along or perpendicular to the inclusion elongation direction and averaged along the direction of acquisition. Crystallographic directions are denoted by square brackets [uvw], specific planes by round brackets (hkl), and families of equivalent planes by curly braces {hkl}.

3. Results

3.1. Mineralogy and petrography of the plagioclase host

3.1.1. Plagioclase in non-altered gabbro

In *non-altered gabbro*, plagioclase forms tabular or more rarely subhedral 0.5–5 mm-sized grains with complex multiple twinning after the Manebach and the Carlsbad twin laws, with internal Albite or Albite-Pericline polysynthetic twinning. These grains show bright blue CL color (Fig. S1 in SM) and are interpreted as primary magmatic. Their anorthite contents range from An#45 to An#60 (andesine/labradorite) and vary over the different plagioclase growth zones. Generally, the

Table 2
Oceanic gabbro samples and the corresponding plagioclase-hosted Fe—Ti oxide micro-inclusions investigated in this study.

	Plagioclase features		Fe-Ti oxide micro-inclusions features				Study methods		Figure No.
	PL zones	# An	Volume pct %	Dominant type	Dominant shape	Category	STEM studied	EBSD studied	
Plagioclase in *non-altered gabbro*	PL_1	#An45–60	<1 vol% of PL_1	plane-normal-type	Needle shape, aspect ratio > 100	70–80 % pl(112)n- & pl($\bar{3}$12)n-mag ~20 % pl(1$\bar{5}$0)n-, pl(150)n-, pl(1$\bar{1}$2)n- & pl($\bar{3}$1$\bar{2}$)n-mag	Lath-shaped pl($\bar{3}$12)n-mag micro-inclusion	–	2a-d, 3–6, S1a
							–	–	2b, c
						~5 % pl[001]-mag	Lath-shaped pl [001]-mag inclusion	–	2d, 8
						< 5 % local vol. pl(100)n-mag	–	–	2b, c
	PL_2, altered zones of PL_1	#An ~5 % lower than PL_1	–	pl[001]-type	Needle shape, aspect ratio varies	–	Lath-shaped pl [001]-mag inclusion in crack	Lath-shaped pl [001]-type inclusion in altered zone of PL_1	1a, 2e, 7a-c, S8
Plagioclase in *altered gabbro*	PL_1, PL_3, PL_4	–	–	pl[001]-type	Short prismatic, aspect ratio < 10	95 % pl[001]-mag 5 % pl(112)n-, pl($\bar{3}$12)n-, pl(100) n-mag type	–	Prismatic pl[001]-type inclusions in PL_1 and PL_3	1b, 2f, 7d-m, 9,10, S1b-c, S2–7
	PL_2	–	–	–	–	–	–	–	–

anorthite content is approximately 5 % lower in the rim zones (PL_2), than in the cores (PL_1). The lowest anorthite contents (down to An#45) are observed along healed cracks (Fig. 1).

The magmatic plagioclase contains Fe—Ti oxide micro-inclusions, which are usually confined to PL_1 and gradually or sharply dwindle towards PL_2. The dominating inclusion type in PL_1 is the plane-normal-type, forming a grid-like pattern of opaque, needle- and lath-shaped micro-inclusions (Fig. 2a-e). At the transition from PL_1 to PL_2 the fraction of pl[001]-type micro-inclusions increases, while the anorthite content decreases. Moreover, healed cracks may contain pl[001]-type micro-inclusions (Fig. 2e), but more often these zones are free of micro-inclusions except for platelets of ilmenite.

3.1.2. *Plagioclase in altered gabbro*

In *altered gabbro,* several generations of plagioclase can be discerned: (i) Early magmatic plagioclase, PL_1, which, similar to PL_1 of *non-altered gabbro*, exhibits bright blue CL (Fig. S1-Fig. S4), but has lower anorthite content, An#39–47. (ii) Late magmatic plagioclase, PL_2, forms the rim zones around PL_1, and shows brighter blue CL and higher anorthite content (An#38–63) than PL_1. This is different from the usual core-to-rim chemical zoning in *non-altered* oceanic gabbro, where the core is more anorthitic than the rim zone. (iii) A later plagioclase generation, PL_3, has intermediate anorthite content (An#50–53) and bright red CL. PL_3 occurs along veinlets of hornblende (Fig. S3) and along healed microcracks in PL_1. PL_3 is never observed as individual newly formed grains, but it always partially replaces PL_1. It is ascribed to HT hydrothermal alteration, accordingly (Pertsev et al., 2015). In addition, a later generation of Na-rich plagioclase PL_4 (An#10) with dark red CL was identified (Fig. S2).

The plagioclase-hosted Fe—Ti oxide micro-inclusions in *altered gabbro* are generally represented by pl[001]-type and are observed in the early magmatic PL_1, including the domains of PL_3 and PL_4, which were affected by hydrothermal alteration. It is difficult to identify a sequence of consecutive plagioclase generations based on the chemical compositions of the altered plagioclase domains. This significantly complicates the assignment of plagioclase generations based on chemical composition. Nevertheless, the CL imaging reveals important patterns and aids localization of these generations and related micro-inclusions. As depicted in the SM Fig. S2-S4, most inclusions are associated with domains of plagioclase exhibiting reddish CL color. Additionally, large inclusions are aligned with healed microcracks that also exhibit red CL color.

We emphasize that the spatial correlation between large micro-inclusions and hydrothermally affected plagioclase was determined based on CL color, as the chemical composition of the plagioclase was uninformative in this case. However, a characteristic chemical pattern was observed: near large Fe—Ti oxide micro-inclusions, the plagioclase host exhibits an elevated anorthite content and reduced Fe content compared to the matrix plagioclase (Fig. 1b, Fig. S2).

3.2. *Phase content and internal microstructures of the Fe—Ti oxide micro-inclusions*

Most micro-inclusions consist of an opaque magnetite matrix intergrown with semi-transparent Ti-bearing oxide lamellae. However, the Fe—Ti oxide micro-inclusions exhibit systematic differences between the two gabbro types in terms of spatial distribution, shape, aspect ratio, phase content, and chemical composition. These characteristics are described below and summarized in Table 2.

3.2.1. *Fe—Ti oxide micro-inclusions in plagioclase from the non-altered gabbro*

Over 1000 plagioclase-hosted Fe—Ti micro-inclusions from *non-altered gabbro* were examined. Based on their spatial distribution and COR relative to the plagioclase host, two distinct types were discerned: plane-normal-type and pl[001]-type inclusions.

3.2.1.1. Plane-normal-type inclusions. The core zones of the plagioclase grains (PL_1) in the *non-altered gabbro* are dominated by the plane-normal-type inclusions, comprising up to 1 vol%. Approximately 80 % of these micro-inclusions have elongation directions closely aligned with the plane-normal directions of the (112) and ($\bar{3}$12) lattice planes of the plagioclase host. Micro-inclusions oriented sub-parallel to the plane normal directions of the (150), (1$\bar{5}$0), (1$\bar{1}$2) and ($\bar{3}$1$\bar{2}$) lattice planes are less abundant (Fig. 2b). In addition, pl[001]-type micro-inclusions are present, but they constitute less than 5 % of all Fe—Ti oxide micro-inclusions in PL_1 in *non-altered gabbro*. In some places, micro-inclusions with their elongation direction oriented parallel to the normal direction of the plagioclase (100) lattice plane are found occupying up to 5 % of the volume. The micro-inclusions observed in PL_1 in

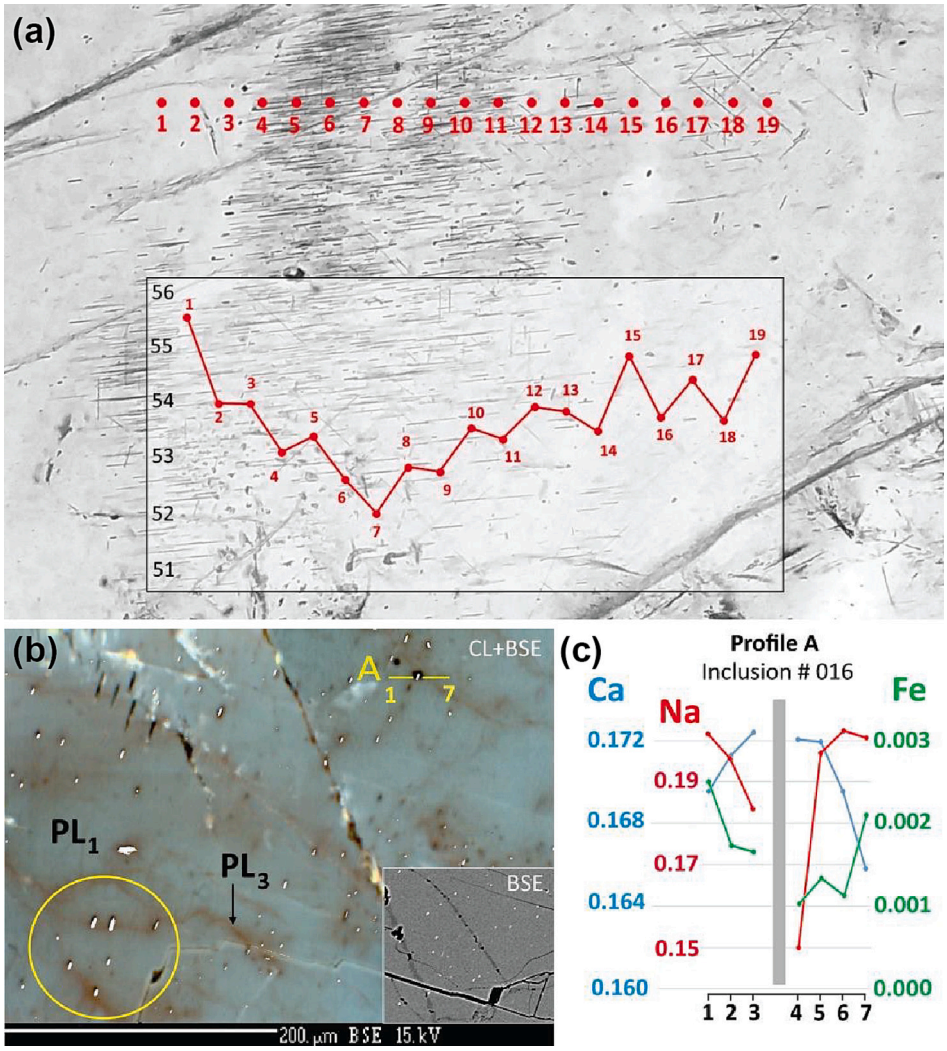

Fig. 1. (a) Optical image and anorthite content (An#) of a plagioclase from *non-altered gabbro* (Sample 277–10), showing regions dominated by pl[001]-type inclusions (points 4–14) and regions dominated by plane-normal inclusions (points 15–19). (b) CL image overlain on a backscattered electron (BSE) image in *altered gabbro*. The early magmatic plagioclase PL_1 is largely inclusion-free or contains only dust-like inclusions. The yellow circle highlights the area where titanomagnetite inclusions are associated with hydrothermally altered plagioclase, characterized by reddish CL color. This fragment is extracted from Fig. S2 in the SM. (c) Chemical profile along line A in (b) showing Ca, Na and Fe contents in plagioclase adjacent to the magnetite-ulvospinel inclusion #016. (For interpretation of the references to color in this figure legend, the reader is referred to the web version of this article.)

non-altered gabbro usually are needle-shaped with high aspect ratios of >100, and they are quite homogeneously distributed within the plagioclase host. Often, these micro-inclusions contain ilmenite lamellae, which were identified based on their chemical compositions from SEM-EDX analysis combined with EBSD analyses yielding excellent indexing statistics when using the reference structure of ilmenite (see methods section). The ilmenite lamellae constitute up to about 15 vol% of the inclusion volume. In addition, extremely thin, <100 nm thick lamellae with different BSE contrast occur in this group of micro-inclusions.

STEM analysis reveals the multiphase nature of the Fe—Ti oxide micro-inclusion (Fig. 3), which is composed of a magnetite matrix intergrown with ilmenite lamellae (Fig. 4a). The lamellae range in width from ~30 nm to ~300 nm. The elongation direction of the inclusion is along one of the mag<111> || pl($\bar{3}$12)n, which identifies it as a pl($\bar{3}$12) n–mag micro-inclusion. Chemical maps and quantitative elemental profiles confirm the identities of the two phases (Figs. 4c–f). Based on the area fractions in Fig. 4a and the negligible thickness of the inclusion, the ilmenite volume fraction is estimated to be <15 %. This estimate is important in the context of exsolution mechanisms in titanomagnetite (Tan et al., 2016).

The ilmenite lamellae are oriented perpendicular to the inclusion elongation direction. The phase boundaries between the ilmenite lamellae and the magnetite matrix are straight and sharp. At the points where magnetite-ilmenite interfaces impinge on the plagioclase host, the plagioclase forms cusps pointing towards the interface, forming microstructurally well-equilibrated triple junctions. These textures suggest local equilibrium and may serve as suitable sites for micro-oxybarometry using Fe—Ti oxide pairs. The accuracy of elemental analysis by STEM EDX applied in this study is too low to allow for meaningful oxybarometry. A coherent, edge-on interface is observed between ilmenite and magnetite within the multiphase inclusion, with an epitaxial relationship defined by (001)⟨010⟩ ilm || {111}⟨112⟩ mag and {100}<010 > ilm || {110}<112 > mag. This orientation relationship is revealed in HAADF-STEM images taken with the viewing direction along the magnetite [112] zone axis, where the magnetite matrix is aligned with [111] in the horizontal and [110] in the vertical direction (Fig. 5). The lattice planes ilm(001) and mag(111) correspond to close-packed oxygen layers in the ilmenite and the magnetite crystal structures (Figs. 5g-h). In this notation, ilm(hkl) refers to the Miller indices (hkl) of lattice planes in the ilmenite structure, following the standard

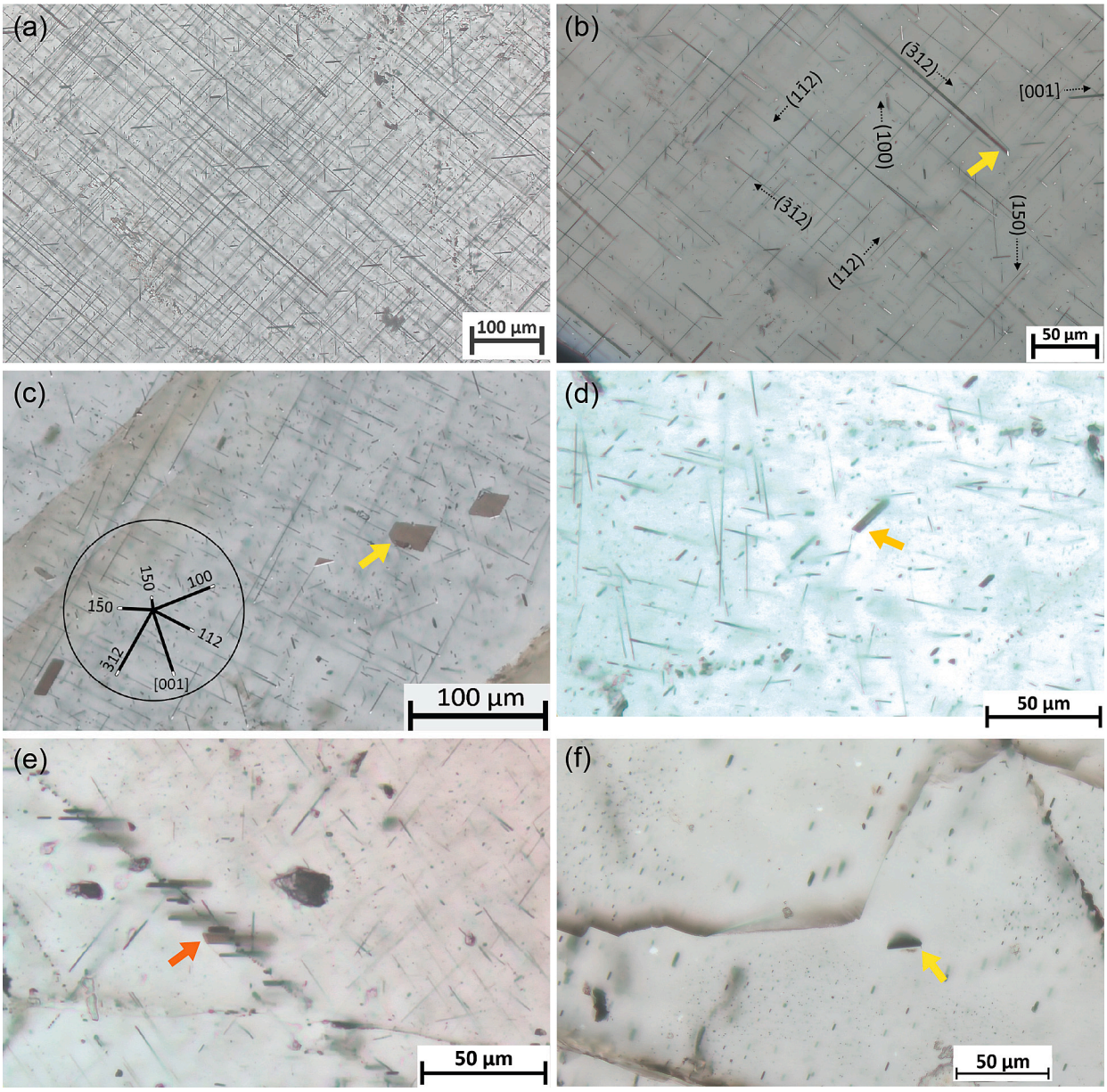

Fig. 2. Optical microscopic images of plagioclase-hosted Fe—Ti oxide micro-inclusions captured in plane-polarized transmitted light (a, d-f) and combined transmitted and reflected light (b, c). Plane-normal-type inclusions with different morphologies: (a) needle, (b) lath and (c) plate shapes. In (b) the orientation classes of the micro-inclusions, determined from EBSD analyses, are marked with the black arrows indicating the elongation directions of the corresponding needle-shaped inclusions. The upper-hemisphere stereographic projection of the corresponding plagioclase grain is embedded in (c). The plagioclase grains in (a-e) are from *non-altered gabbro*: (a-b) Sample 1419–10, (c) Sample L30–277-10, (d-e) Sample 1514–17. (d) Region rich in plane-normal-type inclusions, with several pl[001]-type inclusions; one such inclusion is highlighted by a yellow arrow. (e) Cluster of pl[001]-type inclusions aligned along a healed crack in plagioclase. The thick arrows in each image mark inclusions extracted by FIB for STEM analysis. (f) Plate-shaped ilmenite inclusion in a plagioclase grain from *altered gabbro*. The short prismatic opaque grains are magnetite-(ulvospinel)-ilmenite micro-inclusions of the pl[001]-type. (For interpretation of the references to color in this figure legend, the reader is referred to the web version of this article.)

three-index notation. The alignment of close-packed oxygen layers at the observed interface minimizes structural mismatch and interfacial energy, making it one of the energetically favorable CORs between magnetite and ilmenite. While only one orientation was imaged here, other well-documented CORs involving ilmenite lamellae along magnetite {111} and {100}, and {110} planes may also be present in this system. Fig. 6 presents the left segment of the same inclusion, where the viewing direction is along one of the mag[112] directions, featuring a ~ 300 nm thick ilmenite lamella embedded within a magnetite matrix. In addition, extremely fine lamellae, less than 5 nm thick, are observed on both sides of the thicker ilmenite lamella. Fig. 6c shows a HAADF-STEM image of two fine lamellae adjacent to the thicker ilmenite, while Fig. 6d provides a higher-magnification HAADF-STEM image focusing on one of these fine lamellae. These ultrathin lamellae appear darker than the magnetite matrix and exhibit a crystal structure similar to that of the surrounding magnetite.

The compositional profile in Fig. 6e reveals that the fine lamellae have relatively low Fe and high Ti contents compared to the surrounding magnetite matrix. Notably, the Al content is substantially elevated at the center of the lamella reaching an atomic fraction of about 0.1. Given their structural similarity to the magnetite matrix, along with lower Fe and higher Ti concentrations, these fine, dark-contrast lamellae are inferred to be ulvospinel. However, the elevated Al content in the center of the lamella suggests that in its center the ulvospinel lamella contains

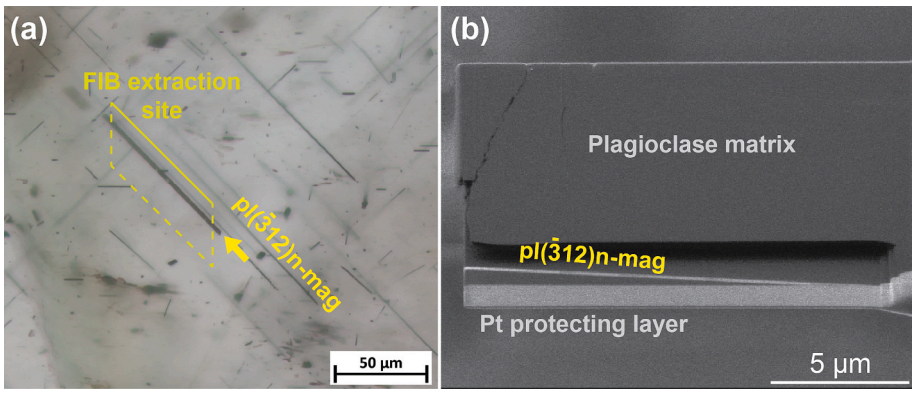

Fig. 3. A pl($\bar{3}$12)n-mag micro-inclusion analyzed using STEM. (a) Optical microscope image of the inclusion, with the FIB extraction site indicated. (b) FIB ion beam image of the foil, showing the inclusion's elongation direction slightly oblique to the trace of the foil.

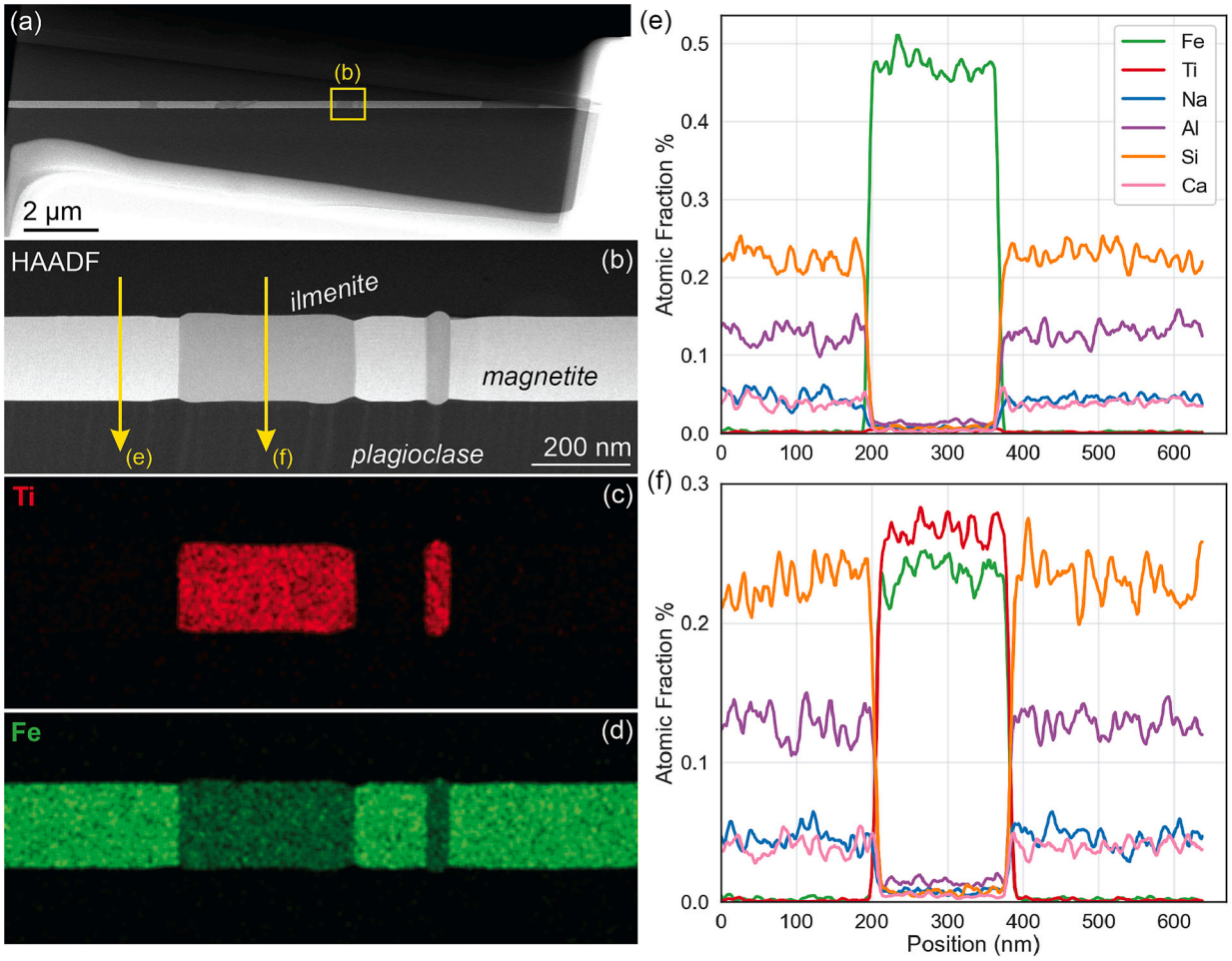

Fig. 4. (a) Overview of the lath-shaped pl($\bar{3}$12)n-mag micro-inclusion with mag⟨111⟩ direction lying horizontally in the plane of the foil. The highlighted segment in (a) contains ilmenite lamellae, shown in detail in the HAADF-STEM image (b). Arrows in (b) indicate the locations and directions of the STEM-EDS line profiles shown in (e,f). (c,d) Ti and Fe distribution maps according to the area in (b). (e,f) Line profiles of major elements atomic fractions along the arrows (e) and (f) indicated in (b).

another lamella with appreciable hercynite ($Fe^{2+}Al_2O_4$) content.

In summary, the lath-shaped pl($\bar{3}$12)n-mag micro-inclusion is primarily composed of magnetite with several 10s to 100 s of nanometers thick lamellae of ilmenite. In addition, comparatively fine, only a few nanometer thick, lamellae of ulvospinel are present, which may be accompanied by similarly fine lamellae with appreciable hercynite content. Both the ilmenite as well as the ulvospinel/hercynite lamellae show specific CORs to the magnetite, and the phase boundaries are usually straight and coherent. The triple junctions at the intersections of the lamellar boundaries with the interface to the plagioclase host are microstructurally well equilibrated.

3.2.1.2. Pl[001]-type inclusions. The regular spatial distribution that is typical for the micro-inclusions of the plane-normal-type in PL_1 is

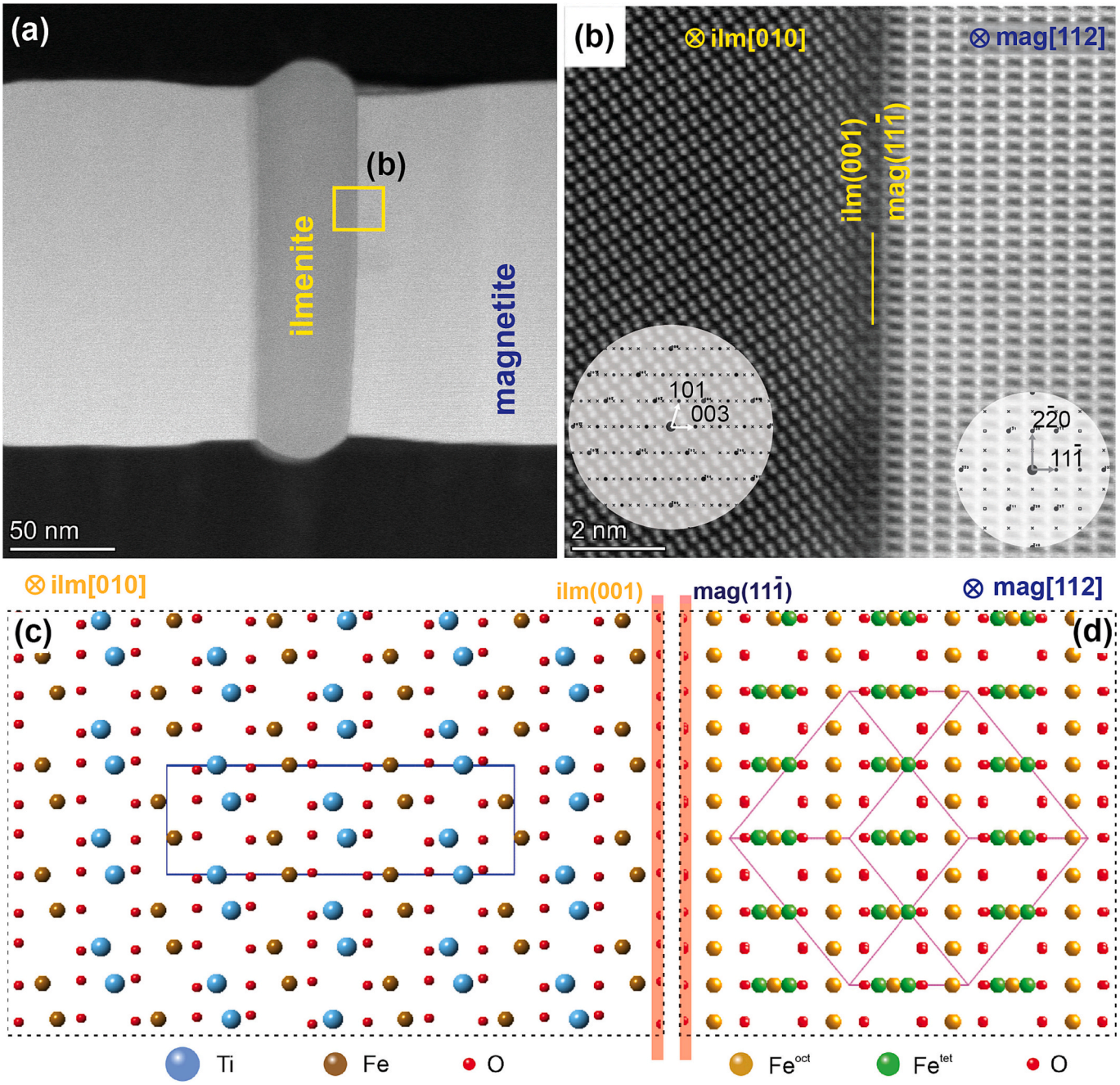

Fig. 5. (a) HAADF-STEM image showing phase boundaries between ilmenite, magnetite, and plagioclase within the lath-shaped pl($\bar{3}$12)n–mag micro-inclusion. The viewing direction is along the mag[112] || ilm[010] zone axis, indicated by the crossed circle symbol (⊗). (b) HAADF-STEM images of ilmenite (left) and magnetite (right), each with a simulated electron diffraction pattern in corresponding orientations as insets. (c, d) Crystal structures and unit cells of ilmenite (Barth and Posnjak, 1934) and magnetite (Fleet, 1981), corresponding to the structures observed in (b).

disrupted in zones surrounding cracks or in the rim zones represented by PL_2. These zones often contain relatively few, dispersed plate-shaped micro-inclusions or abundant micro-inclusions of the pl[001]-type (Fig. 1a, Fig. 2e, Fig. 7a). The pl[001]-type micro-inclusions can be identified by routine petrographic observation: in plagioclase grains, where albite twin boundaries are perpendicular to the thin section surface, the pl[001]-type micro-inclusions, and the much less common pl(100)n-mag micro-inclusions, are aligned parallel to the traces of the albite twin boundaries (Ageeva et al., 2022).

The aspect ratios of the pl[001]-type inclusions are highly variable and, on average, are substantially lower than those of the plane-normal-type inclusions in PL_1. The pl[001]-type micro-inclusions contain rare thin ulvospinel lamellae (~5 vol%), which have been identified based on SEM-EDX and EBSD analysis (Fig. S5). Typically, magnetite and ulvospinel have identical crystallographic orientations, and the magnetite-ulvospinel interfaces are parallel to one of the {100} planes of magnetite and ulvospinel. Figs. 7b-c show the magnetite-ulvospinel boundaries within a pl[001]-type micro-inclusion, along with their crystallographic orientation. (Figs. 7d-m, which refer to pl[001]-type micro-inclusions from *altered gabbro*, will be discussed later.)

As noted above, single inclusions of the pl[001]-type are also observed among plane-normal-type micro-inclusions in PL_1 (Fig. 2d), but they usually constitute less than 5 % of the Fe—Ti oxide micro-inclusions in these domains. A lath-shaped pl[001]–mag micro-

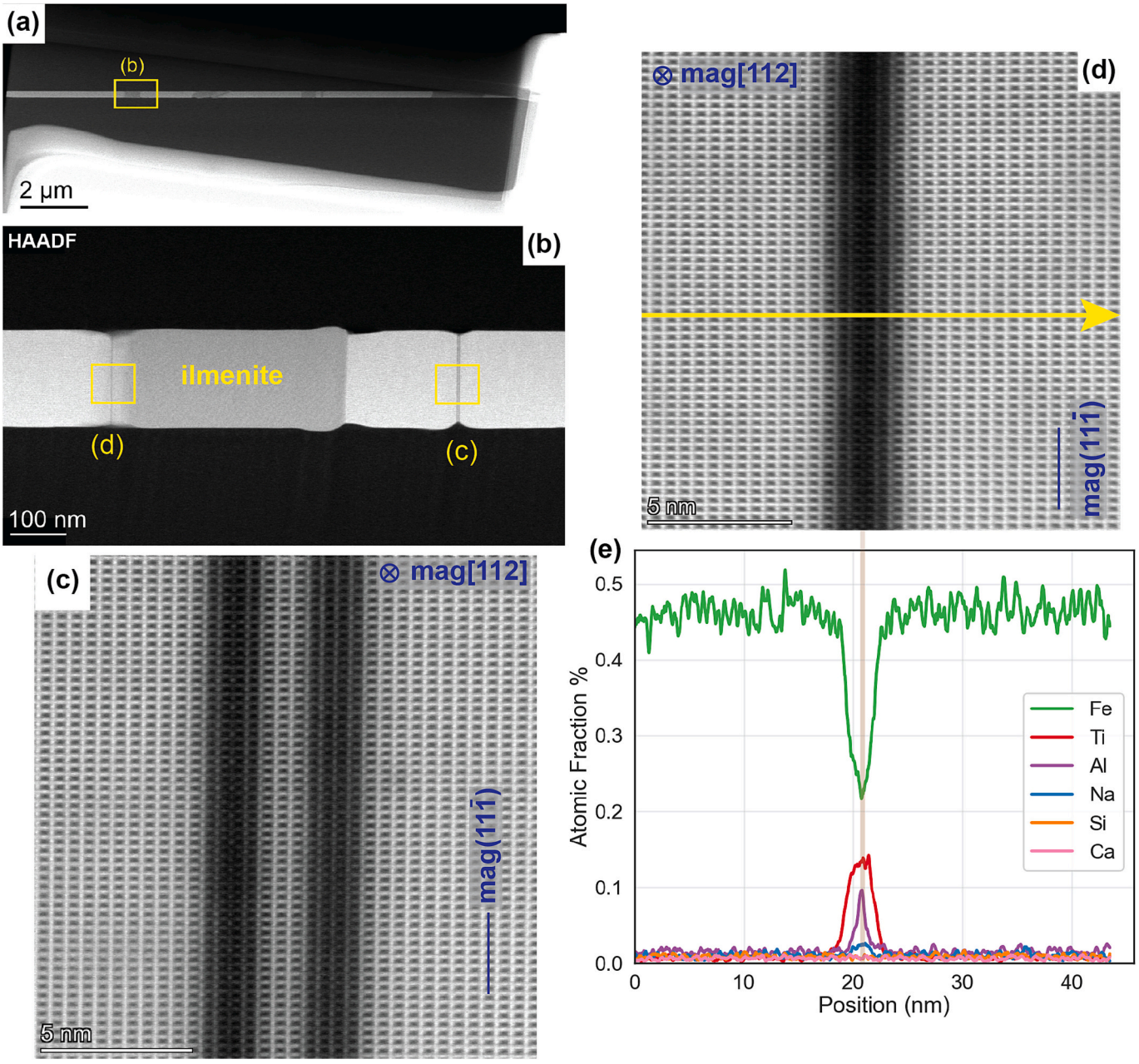

Fig. 6. (a) HAADF-STEM overview image of a lath-shaped pl($\bar{3}$12)n–mag micro-inclusion. (b) Close-up HAADF-STEM image showing an ilmenite lamella and adjacent fine-scale lamellae within the inclusion. The viewing direction is along the mag[112] zone axis (indicated by ⊗). (c, d) HAADF-STEM images revealing the structure of the fine lamellae within the inclusion. (e) Major element atomic fractions along the line profile indicated by the yellow arrow in (d). The alignment of peak positions in the compositional profiles with atomic planes is marked by the brown line. (For interpretation of the references to color in this figure legend, the reader is referred to the web version of this article.)

inclusion with elongation parallel to one of the mag<110> || pl[001] was confirmed through STEM analysis of a FIB foil extracted along its long axis. This inclusion is located in the region dominated by plane-normal-type micro-inclusions and is highlighted in Fig. 2d. Fig. 8 presents a HAADF-STEM image of a section within the micro-inclusion, highlighting lamellae and several semi-circular domains. STEM-EDX compositional profiles along two selected lines are also included. The atomic Fe—Ti ratio confirms that the lamella in Fig. 8a is ilmenite. This ilmenite lamella has an almost hexagonal shape with blurred boundaries to the surrounding magnetite and plagioclase, likely due to the oblique orientation of these interfaces relative to the electron beam. Additionally, the triple junctions, where magnetite-ilmenite interfaces meet the plagioclase host, appear microstructurally well-equilibrated, with the plagioclase forming cusps directed towards the magnetite-ilmenite boundaries. The semi-circular domains within the inclusion exhibit relatively low Fe content, an absence of Ti, and notable Al enrichment, suggesting the possible presence of hercynite.

3.2.2. *Fe—Ti oxide micro-inclusions in plagioclase of altered gabbro*

The Fe—Ti oxide micro-inclusions within plagioclase from *altered gabbro* predominantly belong to the pl[001]-type, accounting for 95 % of the ~200 inclusions examined (Fig. 7d-m, Fig. S6). The shape of the micro-inclusions is short prismatic with aspect ratios <10 (Fig. 9). Rarely inclusions with CORs and SORs corresponding to the pl(112)n-mag, pl($\bar{3}$12)n-mag and pl(100)n-mag types were found, but as opposed to the micro-inclusions in PL_1 from *non-altered gabbro*, they are

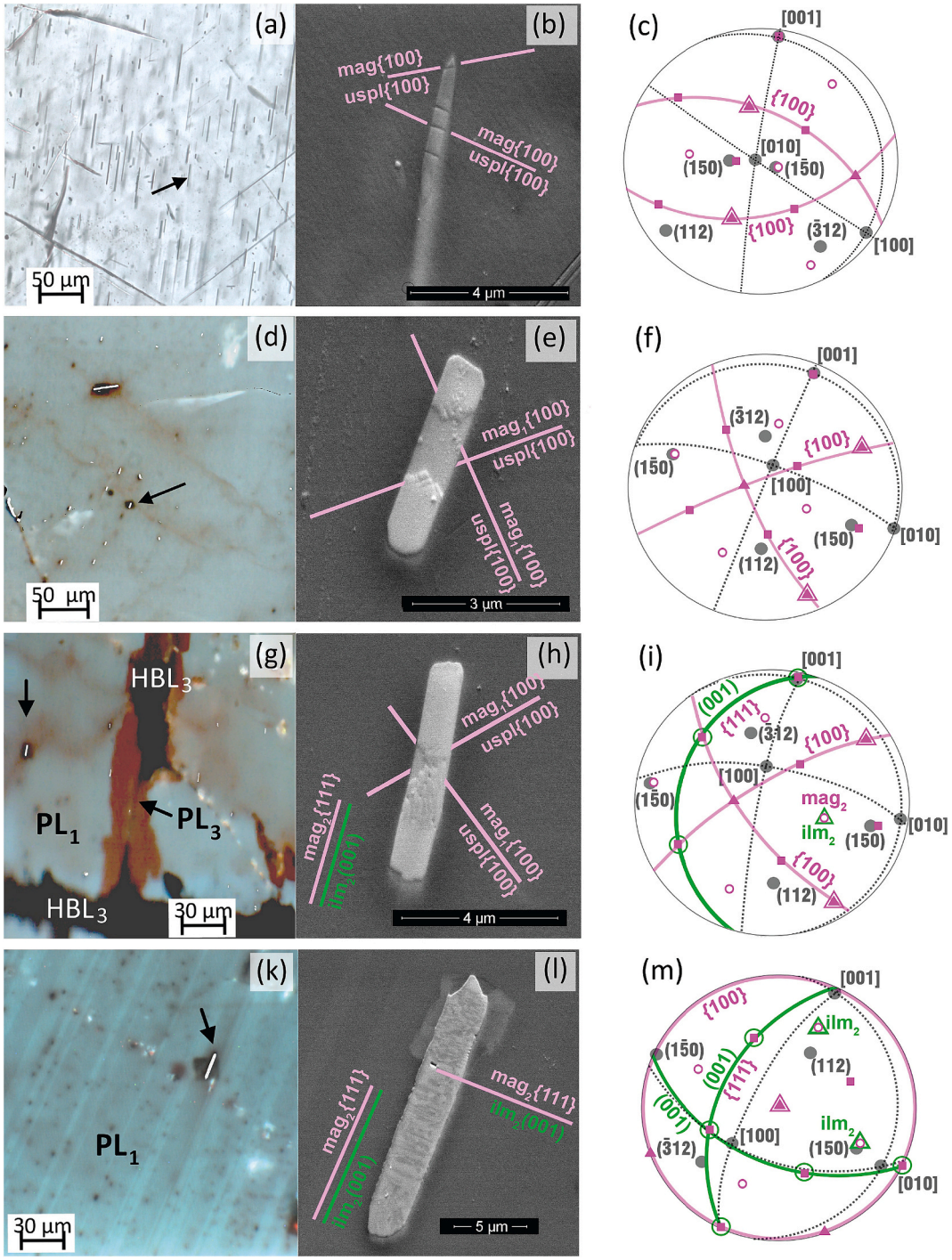

Fig. 7. Optical image (a) CL images combined with SEM images of pl[001]-type micro-inclusions (d,g,k), SEM images (b,e,h,l) and upper hemisphere stereographic projections (c,f,i,m) of the Fe—Ti oxide micro-inclusions from: the Na-rich domains of plagioclase from *non-altered gabbro* (a-c); plagioclase from *altered gabbro* (d-m). The stereographic projections (c,f,i,m) show the CORs between the plagioclase host (grey symbols) and the micro-inclusions: magnetite and ulvospinel (pink symbols: triangle – {100} plane; square – {110} plane; open circle – {111} plane) and ilmenite (green symbols: open triangle – (001) plane; open circle – (100) plane). (a-c): magnetite matrix (mag_1) with rare narrow ulvospinel lamellae (uspl) and mag-uspl phase boundaries oriented parallel to the (001) planes of both minerals (double triangles show the poles of the planes). (d-f): mag_1 + uspl intergrowth with similar CORs and SORs as described for the inclusion type shown in (a-c). Note the low mag/uspl ratio. (g-i) CORs and SORs typical for the inclusion type shown in (a-c) and (d-f) but with fine-grained intergrowths of ilm_2 and mag_2 forming the transition zone between uspl and mag_1 and with (001) of ilm_2 parallel to (111) of mag_1 and mag_2. HBL – HT hydrothermal hornblende (Pertsev et al., 2015). (k-m): coarser-grained mag_2-ilm_2 intergrowth as the inclusion type shown in (g-i). In this grain mag_1 is not observed probably due to a cutting effect: based on position one of the mag{100} poles (double triangle panel (m)), the magnetite-ulvospinel boundary is inferred to be parallel to the surface of the thin section and the mag_1 phase may be hidden under the surface. (For interpretation of the references to color in this figure legend, the reader is referred to the web version of this article.)

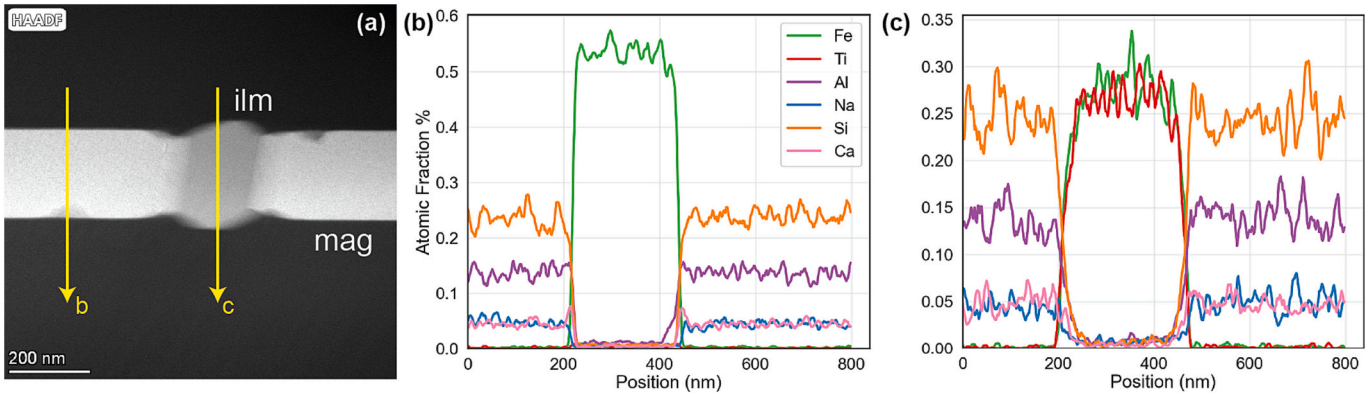

Fig. 8. (a) HAADF-STEM image of a segment in the lath-shaped pl[001]-mag micr-inclusion extracted by FIB parallel to its elongation direction. (b, c) Major element profiles in atomic fractions along the arrows labelled in (a), respectively.

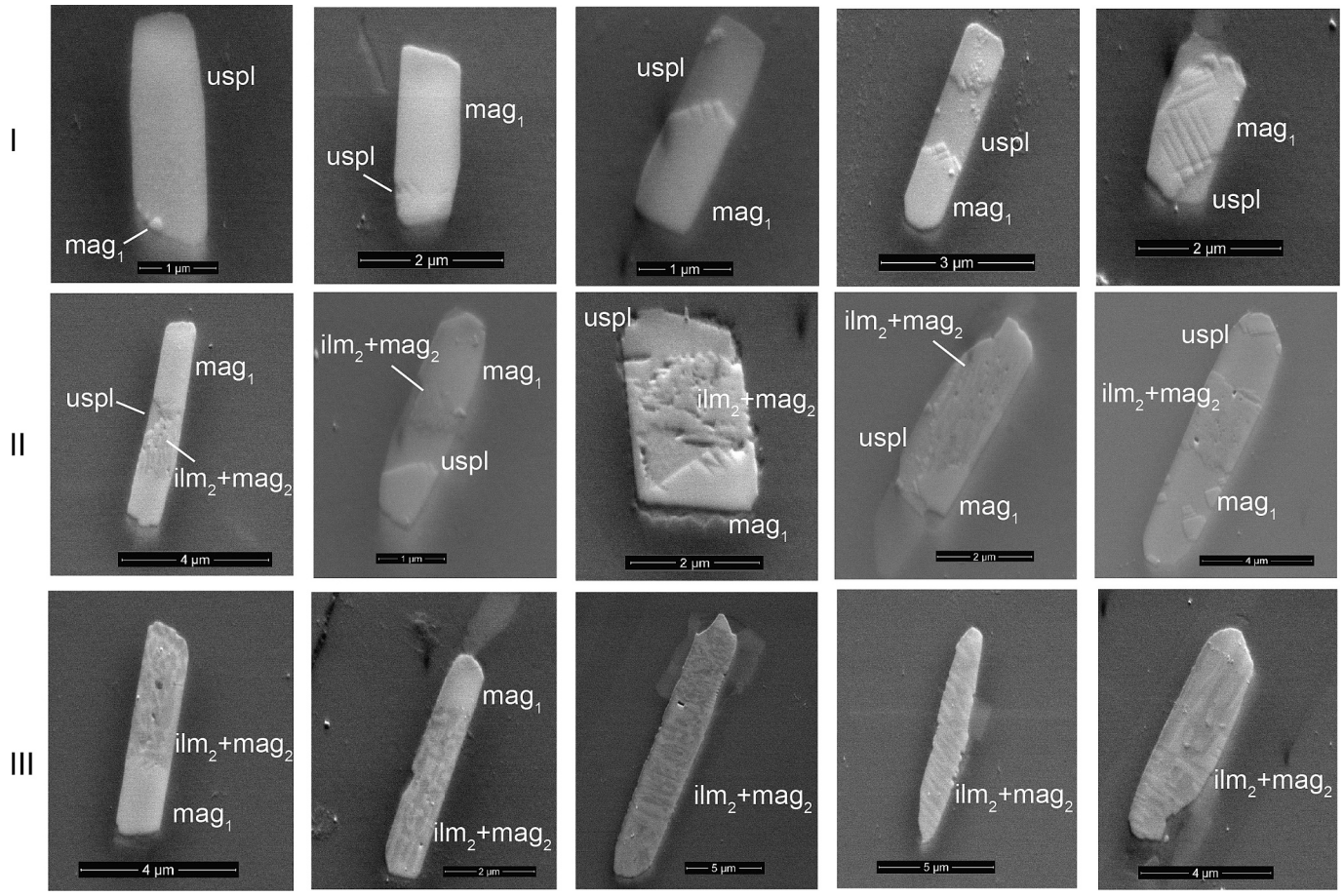

Fig. 9. SEM BSE images of the Fe—Ti oxide micro-inclusions in plagioclase from *altered gabbro*. Magnetite-ulvospinel (row I), magnetite-ilmenite-ulvospinel (row II) and magnetite-ilmenite (row III) micro-inclusions hosted by plagioclase.

characterized by similarly low aspect ratios of <10.

Most of these micro-inclusions are 0.5–1 μm thick and have relatively coarse-grained internal microstructures. They are comprised of a complex intergrowth of magnetite, ulvospinel and ilmenite in different proportions, sizes, and spatial distributions. Based on phase content, three groups of micro-inclusions can be discerned:

(i). The first group is represented by composite magnetite-ulvospinel micro-inclusions, which are usually divided into two or three domains consisting of homogeneous magnetite or homogeneous ulvospinel (Figs. 7d-f, Fig. 9 row I, Fig. 10 row I). In some cases, only one phase may appear on the specimen surface due to cutting effects (Figs. 9 row I first 2 subfigures). We refer to the magnetite domains in this type of intergrowth as mag_1. Elemental mapping on the representative micro-inclusion reveals that the magnetite domains are devoid of Ti and that the ulvospinel domains contain Fe, Ti and a trace amount of Mn (Fig. 10 row I). The areas with elevated concentrations of Mg are due to the presence of another phase, likely pyroxene. Within composite inclusions, mag_1 and uspl have similar CORs to the plagioclase host. The

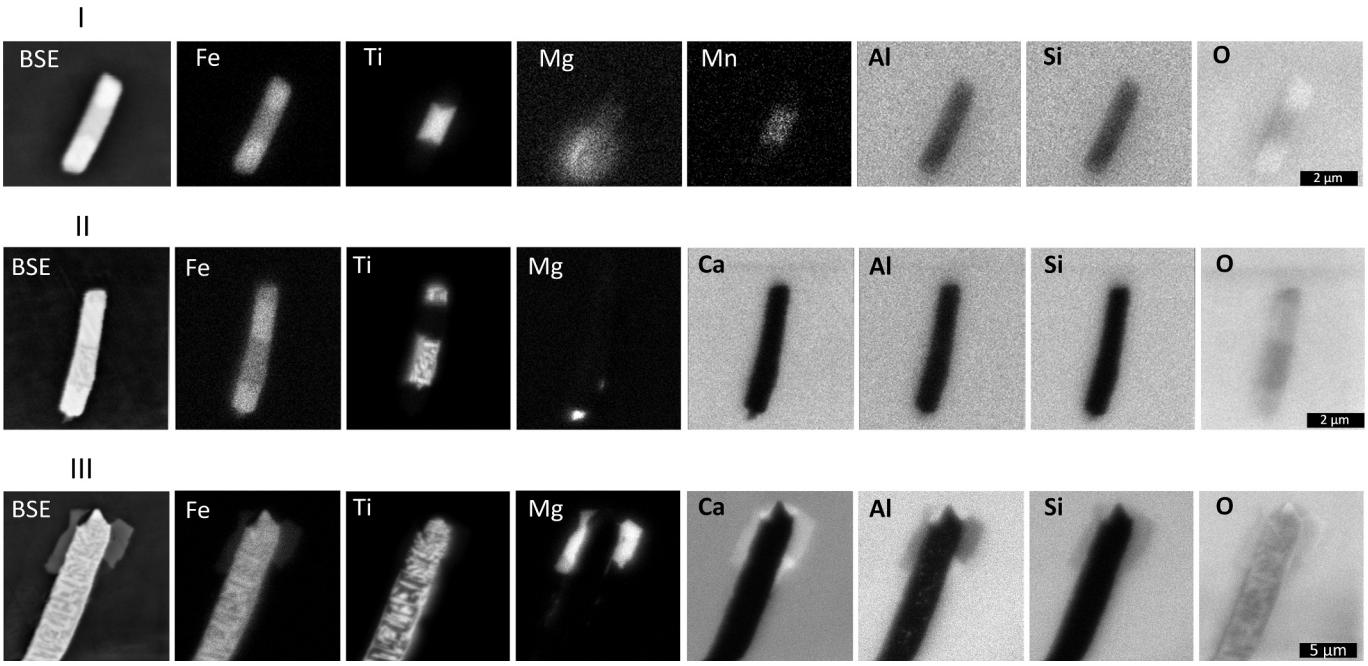

Fig. 10. Element distribution maps for plagioclase-hosted magnetite-ulvospinel (row I), magnetite-ilmenite-ulvospinel (row II), and magnetite-ilmenite (row III) micro-inclusions from *altered gabbro*.

phase boundaries between the phases are straight and their traces are parallel to the traces of the {100} planes of both minerals (Figs. 7e-f). On average, the volume proportion of mag_1 to uspl is approximately 45:55, as estimated from the areal analysis of 20 micro-inclusions exclusively composed of mag_1 and uspl.

(ii). The second group is represented by composite magnetite-ulvospinel-ilmenite micro-inclusions (Figs. 7g-i, Fig. 9 row II, Fig. 10 row II). In addition to the homogeneous mag_1 and uspl domains, these inclusions contain intergrowths of fine-grained magnetite and ilmenite referred to here as mag_2 and ilm_2. On the element distribution maps shown in Fig. 10 row II, the Ti-rich domains correspond to ilmenite, the domains with lower Ti contents correspond to ulvospinel, and the Ti-free domains correspond to magnetite. In addition, ulvospinel shows elevated Al concentrations as compared to magnetite (Fig. S7 upper row). The mag_2 + ilm_2 intergrowths mainly occur within ulvospinel domains and near the contacts to mag_1, and they exhibit a complex microstructure and frequent presence of pores (Figs. 9 row II a,c,e, Fig. S7). Based on these petrographic features, the mag_2 + ilm_2 intergrowths are inferred to be of secondary origin, partially replacing ulvospinel. The phases show specific CORs among each other with the (001) and (100) lattice planes of ilm_2 being parallel to the (111) and (110) lattice planes, respectively, of mag_1 and mag_2, and uspl (Figs. 7g-i). It should be noted that mag_2 and ilm_2 are present at rather similar volume proportions varying between 1/1 and 1/2, which is strongly different from the 6/1 mag/ilm ratio in magnetite-ilmenite intergrowths in the plane-normal-type micro-inclusions typical for plagioclase from *non-altered gabbro*.

(iii). The third group is represented by magnetite-ilmenite inclusions showing an intergrowth of mag_1, mag_2 and ilm_2 with a more coarse-grained internal microstructure (Figs. 7k-m, Fig. 9 row III, Fig. 10 row III). This type of micro-inclusions may have sectors of homogenous mag_1, but ulvospinel sectors are absent. The porosity is lower than in the magnetite-ulvospinel-ilmenite inclusions. The neighboring phases are represented by Al, Ca, Mg, Fe-bearing silicates, presumably amphibole. In addition, an Al-rich phase, supposedly secondary hercynite, forms fine, roundish grains within the mag_2 - ilm_2 aggregates (Fig. 10 row III). Ilmenite shows the same COR with both magnetite generations with (001)<010 > ilm || {111}<112 > mag and {100}< 010 > ilm || {110}<112 > mag. Moreover, the ilmenite-magnetite interfaces align parallel to one of the mag{111} planes (Figs. 7k-m).

4. Discussion

4.1. Specific characteristic of plagioclase-hosted Fe—Ti oxide micro-inclusions

While plagioclase in both *non-altered* and *altered oceanic gabbros* host oriented Fe—Ti oxide micro-inclusions, notable differences exist:

i. Distribution and morphology:

In *non-altered gabbro*, the Fe—Ti oxide micro-inclusions are needle-shaped, uniformly distributed in the core zones of plagioclase (PL_1), and aligned along the plane normal directions of specific plagioclase lattice planes (Figs. 2a-e). *Altered gabbro* shows a more heterogeneous distribution of the Fe—Ti oxide micro-inclusions, with both pl[001]-type and dust-like inclusions in the plagioclase core (Fig. 2f). The pl [001]-type inclusions also occur near cracks and in the outer PL_1 regions in *non-altered gabbro* (Fig. 2e).

ii. Composition and internal microstructure:

In both gabbro types, the Fe—Ti oxide micro-inclusions consist of a magnetite (mag_1) matrix intergrown with more Ti-rich phases (ilmenite or ulvospinel), which supposedly were derived from an originally homogeneous titanomagnetite precursor by exsolution/precipitation. However, the volume proportions between mag_1 and Ti-rich Fe—Ti oxides differ — ~6:1 in *non-altered gabbro* (Bian et al., 2023a) vs. ~1:1 in *altered gabbro*. The internal microstructures of the Fe—Ti oxide micro-inclusions also vary significantly.

iii. Fe—Ti oxide morphology:

Non-altered gabbro features coarse ilmenite and occasional fine ulvospinel lamellae (Figs. 4–6), while in *altered gabbro* ulvospinel domains in mag_1-uspl intergrowth shows rectangular shapes with mag-uspl interfaces parallel to the {100} lattice planes (Fig. 9) and fine-grained mag_2-ilm_2 aggregates (Fig. 10). Magnetite remains pure in both, though ulvospinel contains minor Al (Fig. S7). Fine Al-bearing oxides also appear in mag_2-ilm_2 aggregates in both types (Figs. S7, S8).

These distinctions reflect differing evolutionary paths of the Fe—Ti oxide micro-inclusions in the two gabbro types.

4.2. Evolutionary paths of plagioclase-hosted Fe—Ti oxide micro-inclusions

Microstructural, textural, and chemical data reveal distinct evolutionary paths for the plagioclase-hosted Fe—Ti oxide micro-inclusions from *non-altered* (Path A) and *altered* (Path B) *oceanic gabbro* (Fig. 11). The sub-solidus evolution is divided into several stages:

- Stage I: Homogeneous titanomagnetite (tmag) exsolves from Fe- and Ti-bearing plagioclase at >600 °C (Bian et al., 2021).
- Stage II: In *non-altered gabbro*, the originally homogeneous titanomagnetite exsolves ilmenite during HT oxidation. In *altered gabbro*, titanomagnetite micro-inclusions of the plane-normal-type recrystallize to pl[001]-type inclusions. Stage I-II occur above the T_C of magnetite (~580 °C).
- Stages III–V involve the cooling-induced separation of magnetite and ulvospinel, the formation of secondary magnetite and ilmenite by low-temperature (LT) oxidation of ulvospinel, and the preferred dissolution of magnetite and formation of relic ilmenite during hydrothermal alteration. Stage III-V are inferred to have occurred below the T_C of magnetite.

Based on phase content (magnetite, ilmenite, ulvospinel), the respective volume proportions, spatial distribution (ubiquitous or local), CORs and SORs to the plagioclase host, and grain-internal microstructures, 12 inclusion types are discerned.

4.2.1. Evolutionary path A – stages I and II (inclusion types 1, 2, 4)

In Stage A-I, Fe—Ti oxide micro-inclusions precipitated from Fe- and Ti-bearing plagioclase at temperatures of >600 °C, likely due to changes in redox conditions (Bian et al., 2021). In *non-altered gabbro*, their preservation is indicated by their needle-like shapes, consistent SOR parallel to the normal directions of specific plagioclase lattice planes, and the underlying alignment of densely packed oxygen planes in magnetite with oxygen-rich layers in the plagioclase host (Ageeva et al., 2022; Bian et al., 2023b). Despite later internal transformations, their morphology and orientation identify them as derivatives of HT titanomagnetite.

In Stage A-II the inclusions develop oriented ilmenite lamellae within magnetite (Type-2, Fig. 11), via HT oxidation of titanomagnetite—either by oxy-exsolution at ≥600 °C or direct ilmenite exsolution at ≥900 °C (Lattard, 1995). Rare pl[001]-type inclusions (Fig. 2d) with similarly oriented ilmenite lamellae are also considered primary but are not shown in Fig. 11 due to their rare occurrence.

The primary inclusions may recrystallize during the sub-solidus evolution, especially in hydrothermally altered zones like healed cracks (Bian et al., 2023a), forming pl[001]-type inclusions composed of single-phase Ti-bearing magnetite (mag_{1R}, Type-4, Fig. 11). Their formation temperature—above or below the T_C of magnetite—is unclear; hence, they are placed near the T_C line in Fig. 11 with a question mark.

4.2.2. Evolutionary path A – stages III and IV (inclusion types 3, 5, 6)

As temperature drops, the plane-normal-type Fe—Ti oxide micro-inclusions in *non-altered gabbro* continue to transform (Stage III, Fig. 11). Inclusions like those in Figs. 3–6 contain ilmenite lamellae in a magnetite matrix, with nearby Al-bearing ulvospinel. Ulvospinel exsolution occurred at significantly lower temperatures than ilmenite formation, as is inferred from the low Ti content of magnetite in the light of experimental studies on phase equilibria in the Fe-Ti-O system (Lilova et al., 2012; Lindsley, 1981;Price, 1981; Wei et al., 2020). Moreover, the fact that ilmenite and ulvospinel lamellae are spatially separated in Type-3 inclusions, and isolated ulvospinel lamellae occur as the only lamellar type in Type-5 inclusions corroborates the view that formation

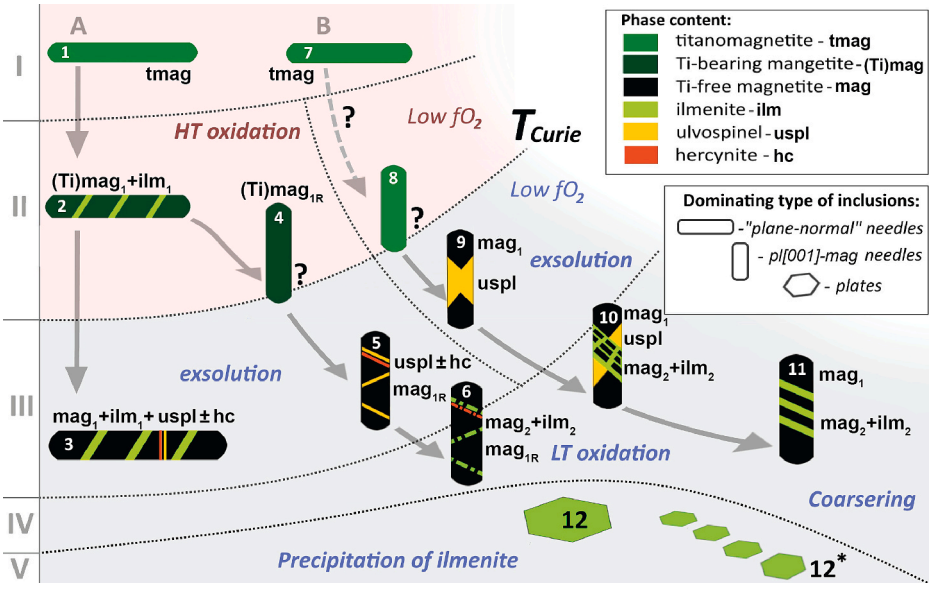

Fig. 11. Summary of evolutionary paths of the plagioclase-hosted Fe—Ti oxides micro-inclusions in *non-altered gabbro* (path A) and *altered gabbro* (path B). The evolutionary stages along each path are labelled with uppercase Roman numerals. HT and LT – high- and low-temperature. T_C - Curie temperature of magnetite ~580 °C. fO_2 - oxygen fugacity. The subscript "1" indicates HT exsolution from titanomagnetite, "R" indicates recrystallization or redeposition, and "2" indicates LT exsolution from titanomagnetite. "?" indicates titanomagnetite and Ti-bearing magnetite that likely existed during early stages but were not preserved in the sample. The numerical labels on the inclusion sketches indicate the type of the inclusion. The varying shades of green in the schematic representations of magnetite reflect changes in Ti concentration: lighter green indicates higher Ti content. Horizontal bars indicate needle-shaped inclusions of the plane-normal-type, vertical bars indicate prismatic pl[001]-type inclusions. (For interpretation of the references to color in this figure legend, the reader is referred to the web version of this article.)

of ilmenite at temperatures >600 °C from HT oxidation and ulvospinel at temperatures below 450–600 °C induced by cooling occurred sequentially. The localized Al enrichment observed in one of the investigated ulvospinel lamellae suggests that hercynite exsolution may have occurred during this stage.

Ulvospinel exsolution also occurs in secondary pl[001]-type inclusions (mag_{1R}, Fig. S5), found typically at transition zones between PL_1 and PL_2 (Figs. 1a, 2e). These inclusions are composed of mag_{1R} with uspl lamellae and are classified as Type-5.

In Stage IV, further cooling leads to LT oxidation of the ulvospinel lamellae, which produces fine-grained mag_2-ilm_2 aggregates within a matrix of mag_{1R}. The LT oxidation of ulvospinel may be written as:

$$6\ Fe_2TiO_4\ (100\%uspl) + O_2 = 6\ FeTiO_3\ (68\ vol\%ilm) + 2\ Fe_3O_4\ (32\ vol\%mag) \quad (1)$$

This yields a modal ilm/mag ratio of ~2:1, defining Type-6 inclusions (Fig. 11), whose structure is further discussed in relation to the evolution of *altered gabbro*.

4.2.3. Evolutionary path B – stages I–II (inclusion types 7, 8, 9)

Like Path A, Path B in *altered gabbro* presumably starts with the precipitation of homogeneous titanomagnetite of the plane-normal-type (Type-7) from Fe- and Ti-bearing plagioclase at temperatures of >600 °C, Stage B—I (Bian et al., 2021, Bian et al., 2023a, 2023b). In *altered gabbro*, pl[001]-type inclusions dominate, while plane-normal-types are rare. This likely reflects recrystallization of primary inclusions of the plane-normal-type (Type-7) and/or direct precipitation of pl[001]-types, influenced by HT hydrothermal alteration (Bian et al., 2023a; Pertsev et al., 2015). Either one of these routes ultimately led to the formation of short prismatic titnaomagnetite inclusions classified as Type-8 ($tmag_R$, Fig. 11).

At high temperatures, above about 455–600 °C, titanomagnetite shows complete miscibility between the magnetite and the ulvospinel end members. Towards lower temperatures, a miscibility gap opens (Price, 1981; Lindsley, 1981; Lilova et al., 2012; Arguin et al., 2018; Wei et al., 2020). Upon cooling from supersovlus temperatures, titanomagnetite of intermediate composition crosses the solvus at about 455–600 °C (Price, 1981; Wei et al., 2020), and exsolution into ulvospinel and Ti-poor magnetite is expected to occur below these temperatures.

Accordingly, the Type-8 titanomagnetite inclusions exsolve into composites of Ti-poor magnetite and ulvospinel during cooling, giving rise to inclusions of Type-9 (Fig. 11). The Type-9 inclusions show ulvospinel to magnetite volume proportions of ~45:55 (Fig. S9), indicating that the precursor titanomagnetite (Type-8) had intermediate compositions. The Type-8 inclusions originally formed at supersolvus temperatures likely during HT hydrothermal alterations. As their formation may have occurred above or below T_C of magnetite, they are plotted across both Stages B-II and B-III in Fig. 11.

The high Ti content in Type-8 inclusions cannot result directly from the primary Fe—Ti oxide micro-inclusions precipitated from plagioclase, because the plagioclase host typically has low-Ti contents and low Ti/Fe ratios, making the first Fe—Ti oxide precipitates also relatively Ti poor. This is reflected by the inclusions formed along Path A, which typically have ≤15 vol% ilmenite. The comparatively high Ti contents of Type-8 inclusions likely reflect preferential dissolution of the magnetite component and removal of Fe during HT hydrothermal overprint. Their location along microcracks and twin boundaries (Fig. 1b) supports fluid-mediated processing. Due to the notoriously low mobility of Ti in hydrothermal systems (Antignano and Manning, 2008), fluid-mediated input of Ti from an external source is considered highly unlikely.

Finally, the absence of oriented ilmenite lamellae in Type-8 inclusions indicates more reducing conditions during the early evolutionary stages (Stages I and II) along Path B, preventing HT oxidation, which is typical for Path A. This interpretation aligns with the petrogenetic history of the altered gabbro, where reducing conditions were inferred for the transition from the magmatic to HT hydrothermal stages (Pertsev et al., 2015).

4.2.4. Evolutionary path B – stages III–IV (inclusion types 8–11)

In Stage B-III, single-phase titanomagnetite ($tmag_R$, Type-8) underwent cooling-induced exsolution into magnetite (mag_1) and ulvospinel, forming the two-phase Type-9 inclusions (Fig. 11). In these inclusions magnetite and ulvospinel share the same crystallographic orientation, with their phase boundaries typically along the {100} planes (Figs. 7e, h). The intergrowths between ulvospinel and Ti-poor magnetite are rectilinear (Fig. 9 row I, Fig. 10 row I) and can fully occupy the inclusion (Fig. 9 row I) or persist as relics within aggregates (Fig. 9 row II). The observed ulvospinel-to-magnetite volume ratio of approximately 45:55 (Fig. S9) suggests that exsolution likely occurred below 450–550 °C. Therefore, the formation of Type-9 micro-inclusions can be confidently attributed to temperatures below the Curie point.

During Stage B-IV, ulvospinel in Type-9 inclusions was partially or completely replaced by fine-grained vermicular intergrowths of mag_2 and ilm_2 aggregates, indicating LT oxidation. In Type-10 inclusions, relics of ulvospinel are preserved (Figs. 7h, 9 row II, 10 row II); in Type-11 inclusions, the ulvospinel was entirely replaced by mag_2-ilm_2 aggregates (Figs. 7l, 9 row III, 10 row III). The LT oxidation of ulvospinel typically starts at mag_1-uspl interfaces.

Where mag_2 and ilm_2 coarsened (Fig. S2, grains #012–014), their volume ratio (~2:1) matches predictions from LT oxidation (Eq. (1)). Due to a slightly higher Al content in ulvospinel than in magnetite (Fig. S7), its breakdown also formed a separate Al-rich phase, visible as scattered Al-rich grains in the aggregates (Figs. 10, S7, S8).

Microcracks in the plagioclase host that once allowed for the infiltration of HT fluids driving formation of Type-8 inclusions likely later enabled oxidizing fluids to enter, driving the LT oxidation of ulvospinel and its replacement by mag_2 and ilm_2 aggregates.

4.2.5. Stage V

In both types of gabbro, plate-shaped single-phase ilmenite inclusions (Type-12 and 12* in Fig. 11) occur in inclusion-poor zones of plagioclase. These ilm_R inclusions likely formed through selective dissolution of magnetite and the removal of Fe during hydrothermal processing. Petrographic evidence suggests that they originated from ilmenite lamellae exsolved during HT oxidation (Stage A-II) or LT oxidation of ulvospinel (Stage B-IV). Their formation likely involved fluid-mediated recrystallization and coalescence of the residual ilmenite grains.

4.3. Implications

The progression from plane-normal-type to pl[001]-type micro-inclusions and the evolution of the phase contents and grain-internal microstructures of the Fe—Ti oxide micro-inclusions reflect a complex interplay between primary supposedly late magmatic crystallization, cooling, and secondary hydrothermal overprint. These processes may influence the magnetic properties of intrusive rocks not only in the oceanic crust but also, potentially, across a broader range of geological settings, including layered intrusions and mafic plutonic suites.

By linking micro-inclusions in plagioclase to broader trends observed in mafic rocks, this work contributes to a more integrated understanding of Fe—Ti oxide behavior in magmatic and hydrothermal systems. It supports interpretations of redox evolution, mineral-fluid interaction, and crystallization pathways in oceanic crustal settings. Moreover, the results refine geochemical models on the evolution of Fe—Ti oxide and provide reference textures and mineral assemblages that can inform studies of cooling rates, alteration intensity, and fluid pathways in mafic intrusive rocks.

5. Conclusions

Two types of oceanic gabbro exhibit contrasting sub-solidus and hydrothermal evolution, resulting in distinct pathways for the formation and transformation of plagioclase-hosted Fe—Ti oxide micro-inclusions. In *non-altered gabbro*, primary Fe—Ti oxide micro-inclusions formed by precipitation of titanomagnetite from Fe- and Ti-bearing plagioclase at temperatures above 600 °C and evolved through HT oxidation and LT exsolution. These inclusions likely carry TRM, with minor overprinting from later hydrothermal alteration.

In contrast, *altered gabbro* underwent more intense hydrothermal processing, leading to the predominance of pl[001]-type inclusions, which formed or recrystallized under reducing conditions, bypassing HT oxidation. Cooling-induced exsolution and subsequent LT oxidation occurred below the T_C of magnetite, producing complex magnetite–ulvospinel–ilmenite textures. The resulting inclusions acquired CRM during these stages.

The contrasting thermal and redox histories of the two gabbros control the timing, mineralogy, and magnetic properties of their Fe—Ti oxide micro-inclusions. These differences have significant implications for interpreting the remanent magnetization of oceanic lower crustal rocks.

Declaration of competing interest

The authors declare that they have no known competing financial interests or personal relationships that could have appeared to influence the work reported in this paper.

Credit authorship contribution statement

Ge Bian: Writing – original draft, Visualization, Methodology, Investigation, Formal analysis, Data curation, Conceptualization. **Olga Ageeva:** Writing – review & editing, Visualization, Investigation, Funding acquisition, Formal analysis, Conceptualization. **Alexey Pertsev:** Writing – review & editing, Resources. **Andras Kovacs:** Writing – review & editing, Investigation. **Gerlinde Habler:** Writing – review & editing, Investigation. **Qianqian Lan:** Writing – review & editing. **Rafal E. Dunin-Borkowski:** Writing – review & editing, Investigation. **Olga Zhilicheva:** Writing – review & editing, Investigation. **Rainer Abart:** Writing – review & editing, Supervision, Project administration, Funding acquisition, Conceptualization.

Acknowledgements

Funding by the Austrian Science Foundation (FWF), Grant No. I 3998 N29 and Russian Foundation for Basic Research (RFBR), Grant No. 18-55-14003 are gratefully acknowledged. This project has received funding from the European Union's Horizon 2020 research and innovation programme under grant agreement No 823717 – ESTEEM3.

Appendix A. Supplementary data

Supplementary data to this article can be found online at https://doi.org/10.1016/j.lithos.2025.108211.

References

Ageeva, O., Habler, G., Topa, D., Waitz, T., Li, C., Pertsev, A., Griffiths, T., Zhilicheva, O., Abart, R., 2016. Plagioclase hosted Fe-Ti-oxide micro-inclusions in an oceanic gabbro-plagiogranite association from the Mid Atlantic ridge at 13°34' N. Am. J. Sci. 316, 85–109. https://doi.org/10.2475/02.2016.01.

Ageeva, O., Habler, G., Pertsev, A., Abart, R., 2017. Fe-Ti oxide micro-inclusions in clinopyroxene of oceanic gabbro: phase content, orientation relations and petrogenetic implication. Lithos 290–291, 104–115. https://doi.org/10.1016/j.lithos.2017.08.007.

Ageeva, O., Bian, G., Habler, G., Pertsev, A., Abart, R., 2020. Crystallographic and shape orientations of magnetite micro-inclusions in plagioclase. Contrib. Mineral. Petrol. 175, 95. https://doi.org/10.1007/s00410-020-01735-8.

Ageeva, O., Habler, G., Gilder, S.A., Schuster, R., Pertsev, A., Pilipenko, O., Bian, G., Abart, R., 2022. Oriented magnetite inclusions in plagioclase: implications for the anisotropy of magnetic remanence. Geochem. Geophys. Geosyst. 23, e2021GC010272. https://doi.org/10.1029/2021GC010272.

Antignano, A., Manning, C.E., 2008. Rutile solubility in H2O, H2O–SiO2, and H2O–NaAlSi3O8 fluids at 0.7–2.0 GPa and 700–1000 °C: implications for mobility of nominally insoluble elements. Chem. Geol. 255, 283–293. https://doi.org/10.1016/j.chemgeo.2008.07.001.

Arguin, J.P., Pagé, P., Barnes, S.J., Girard, R., Duran, C., 2018. An intergrated model for ilmenite, Al-spinel, and corundum exsolutions in titanomagnetite from oxide-rich layers of the Lac Doré Complex (Québec, Canada). Minerals 8 (11), 476. https://doi.org/10.3390/min8110476.

Auzende, J.-M., Bideau, D., Bonatti, E., Cannat, M., Honnorez, J., Lagabrielle, Y., Malavieille, J., Mamaloukas-Frangoulis, V., Mevel, C., 1989. Direct observation of a section through slow-spreading oceanic crust. Nature 337, 726–729. https://doi.org/10.1038/337726a0.

Barth, T.F., Posnjak, E., 1934. The Crystal Structure of Ilmenite. Zeitschr. Kristallogr. Crystall. Mater. 88 (1–6), 265–270.

Bian, G., Ageeva, O., Rečnik, A., Habler, G., Abart, R., 2021. Formation pathways of oriented magnetite micro-inclusions in plagioclase from oceanic gabbro. Contrib. Mineral. Petrol. 176, 104. https://doi.org/10.1007/s00410-021-01864-8.

Bian, G., Ageeva, O., Roddatis, V., Habler, G., Schreiber, A., Abart, R., 2023a. Oriented secondary magnetite micro-inclusions in plagioclase from oceanic gabbro. Am. Mineral. 108, 1642–1657. https://doi.org/10.2138/am-2022-8784.

Bian, G., Ageeva, O., Roddatis, V., Li, C., Pennycook, T.J., Habler, G., Abart, R., 2023b. Crystal structure controls on oriented primary magnetite micro-inclusions in plagioclase from oceanic gabbro. J. Petrol. 64, egad008. https://doi.org/10.1093/petrology/egad008.

Bonatti, E., Ligi, M., Brunelli, D., Cipriani, A., Fabretti, P., Ferrante, V., Gasperini, L., Ottolini, L., 2003. Mantle thermal pulses below the Mid-Atlantic Ridge and temporal variations in the formation of oceanic lithosphere. Nature 423, 499–505. https://doi.org/10.1038/nature01594.

Bonatti, E., Brunelli, D., Buck, W.R., Cipriani, A., Fabretti, P., Ferrante, V., Gasperini, L., Ligi, M., 2005. Flexural uplift of a lithospheric slab near the Vema transform (Central Atlantic): timing and mechanisms. Earth Planet. Sci. Lett. 240, 642–655. https://doi.org/10.1016/j.epsl.2005.10.010.

Brunelli, D., Sanfilippo, A., Bonatti, E., Skolotnev, S., Escartin, J., Ligi, M., Ballabio, G., Cipriani, A., 2020. Origin of oceanic ferrodiorites by injection of nelsonitic melts in gabbros at the Vema Lithospheric Section, Mid Atlantic Ridge. Lithos 368–369, 105589. https://doi.org/10.1016/j.lithos.2020.105589.

Champness, P.E., 1970. Nucleation and growth of iron oxides in olivines, (Mg,Fe)2SiO4. Mineral. Mag. 37, 790–800. https://doi.org/10.1180/minmag.1970.037.291.05.

Cipriani, A., Bonatti, E., Brunelli, D., Ligi, M., 2009. 26 million years of mantle upwelling below a segment of the Mid Atlantic Ridge: the Vema Lithospheric Section revisited. Earth Planet. Sci. Lett. 285, 87–95. https://doi.org/10.1016/j.epsl.2009.05.046.

Dunlop, D.J., Özdemir, Ö., 1997. Rock Magnetism: Fundamentals and Frontiers, Cambridge Studies in Magnetism. Cambridge University Press, Cambridge. https://doi.org/10.1017/CBO9780511612794.

Feinberg, J.M., Harrison, R.J., Kasama, T., Dunin-Borkowski, R.E., Scott, G.R., Renne, P. R., 2006. Effects of internal mineral structures on the magnetic remanence of silicate-hosted titanomagnetite inclusions: an electron holography study. J. Geophys. Res. Solid Earth 111. https://doi.org/10.1029/2006JB004498.

Ferré, E.C., Kupenko, I., Martín-Hernández, F., Ravat, D., Sanchez-Valle, C., 2021. Magnetic sources in the Earth's mantle. Nat. Rev. Earth Environ. 2, 59–69. https://doi.org/10.1038/s43017-020-00107-x.

Fleet, M.E., 1981. The structure of magnetite. Struct. Sci. 37 (4), 917–920. https://doi.org/10.1107/S0567740881004597.

Gao, W., Ciobanu, C.L., Cook, N.J., Slattery, A., Huang, F., Wang, D., 2019. Nanoscale study of lamellar exsolutions in clinopyroxene from olivine gabbro: recording crystallization sequences in iron-rich layered intrusions. Am. Mineral. 104, 244–261. https://doi.org/10.2138/am-2019-6764.

Hooft, E.E.E., Detrick, R.S., Toomey, D.R., Collins, J.A., Lin, J., 2000. Crustal thickness and structure along three contrasting spreading segments of the Mid-Atlantic Ridge, 33.5°–35°N. J. Geophys. Res. Solid Earth 105, 8205–8226. https://doi.org/10.1029/1999JB900442.

Hwang, S.-L., Shen, P., Yui, T.-F., Chu, H.-T., 2010. On the coherency-controlled growth habit of precipitates in minerals. J. Appl. Crystallogr. 43, 417–428. https://doi.org/10.1107/S0021889810007454.

Hwang, S.-L., Shen, P., Yui, T.-F., Chu, H.-T., Usui, Y., 2024. A transmission electron microscopy study of the crystallographic characteristics of magnetite needles in plagioclase. J. Appl. Crystallogr. 57, 71–87. https://doi.org/10.1107/S160057672301004X.

Kato, C., Usui, Y., Sato, M., 2024. A brief review of single silicate crystal paleointensity: rock-magnetic characteristics, mineralogical backgrounds, methods and applications. Earth Planets Space 76, 49. https://doi.org/10.1186/s40623-024-01994-w.

Knafelc, J., Filiberto, J., Ferré, E.C., Conder, J.A., Costello, L., Crandall, J.R., Dyar, M.D., Friedman, S.A., Hummer, D.R., Schwenzer, S.P., 2019. The effect of oxidation on the mineralogy and magnetic properties of olivine. Am. Mineral. 104, 694–702. https://doi.org/10.2138/am-2019-6829.

Lattard, D., 1995. Experimental evidence for the exsolution of ilmenite from titaniferous spinel. Am. Mineral. 80, 968–981. https://doi.org/10.2138/am-1995-9-1013.

Lilova, K.I., Pearce, C.I., Gorski, C., Rosso, K.M., Navrotsky, A., 2012. Thermodynamics of the magnetite-ulvöspinel (Fe3O4-Fe2TiO4) solid solution. Am. Mineral. 97, 1330–1338. https://doi.org/10.2138/am.2012.4076.

Lindsley, D.H., 1981. Some experiments pertaining to the magnetite-ulvospinel miscibility gap. Am. Mineral. 66, 759–762.

Nikolaisen, E.S., Harrison, R., Fabian, K., Church, N., McEnroe, S.A., Sørensen, B.E., Tegner, C., 2022. Hysteresis parameters and magnetic anisotropy of silicate-hosted magnetite exsolutions. Geophys. J. Int. 229, 1695–1717. https://doi.org/10.1093/gji/ggac007.

Ondréas, H., Cannat, M., Fouquet, Y., Normand, A., 2012. Geological context and vents morphology of the ultramafic-hosted Ashadze hydrothermal areas (Mid-Atlantic Ridge 13°N). Geochem. Geophys. Geosyst. 13. https://doi.org/10.1029/2012GC004433.

Peirce, C., Reveley, G., Robinson, A.H., Funnell, M.J., Searle, R.C., Simão, N.M., MacLeod, C.J., Reston, T.J., 2019. Constraints on crustal structure of adjacent OCCs and segment boundaries at 13°N on the Mid-Atlantic Ridge. Geophys. J. Int. 217, 988–1010. https://doi.org/10.1093/gji/ggz074.

Peirce, C., Robinson, A.H., Funnell, M.J., Searle, R.C., MacLeod, C.J., Reston, T.J., 2020. Magmatism versus serpentinization—crustal structure along the 13°N segment at the Mid-Atlantic Ridge. Geophys. J. Int. 221, 981–1001. https://doi.org/10.1093/gji/ggaa052.

Pertsev, A.N., Bortnikov, N.S., Aranovich, L.Ya., Vlasov, E.A., Beltenev, V.E., Ivanov, V. N., Simakin, S.G., 2009. Peridotite-melt interaction under transitional conditions between the spinel and plagioclase facies beneath the Mid-Atlantic Ridge: Insight from peridotites at 13°N. Petrology 17, 124–137. https://doi.org/10.1134/S0869591109020027.

Pertsev, A.N., Aranovich, L.Y., Prokofiev, V.Y., Bortnikov, N.S., Cipriani, A., Simakin, S. S., Borisovskiy, S.E., 2015. Signatures of residual melts, magmatic and seawater-derived fluids in oceanic lower-crust gabbro from the vema lithospheric section, Central Atlantic. J. Petrol. 56, 1069–1088. https://doi.org/10.1093/petrology/egv028.

Price, G.D., 1981. Subsolidus phase relations in the titanomagnetite solid solution series. Am. Mineral. 66, 751–758.

Renne, P.R., Scott, G.R., Glen, J.M.G., Feinberg, J.M., 2002. Oriented inclusions of magnetite in clinopyroxene: source of stable remanent magnetization in gabbros of the Messum complex, Namibia. Geochem. Geophys. Geosyst. 3, 1–11. https://doi.org/10.1029/2002GC000319.

Sholukhov, K.N., Prokofiev, V.Yu., Solovova, I.P., Borisovsky, S.E., Zhilicheva, O.M., Pertsev, A.N., 2022. Residual melt after the crystallization of oxide gabbro: an example of a silicic product of MORB differentiation in the modern oceanic crust, Ashadze complex, Central Atlantic. Petrology 30, 25–39. https://doi.org/10.1134/S0869591122010076.

Sobolev, P.O., 1990. Orientation of acicular iron-ore mineral inclusions in plagioclase. Int. Geol. Rev. 32, 616–628. https://doi.org/10.1080/00206819009465804.

Tan, Wei, Liu, Peng, He, Hongping, Wang, Christina Y., Liang, Xiaoliang, 2016. Mineralogy and origin of exsolution in Ti-rich magnetite from different magmatic Fe-ti oxide-bearing intrusions. Can. Mineral. 54 (3), 539–553. https://doi.org/10.3749/canmin.1400069.

Wei, Y., Niu, Y., Gong, H., Duan, M., Chen, S., Guo, P., Sun, P., 2020. Geochemistry and iron isotope systematics of coexisting Fe-bearing minerals in magmatic FeTi deposits: a case study of the Damiao titanomagnetite ore deposit, North China Craton. Gondwana Res. 81, 240–251. https://doi.org/10.1016/j.gr.2019.12.001.

Wenk, H.-R., Chen, K., Smith, R., 2011. Morphology and microstructure of magnetite and ilmenite inclusions in plagioclase from Adirondack anorthositic gneiss. Am. Mineral. 96, 1316–1324. https://doi.org/10.2138/am.2011.3760.

Wolfe, C.J., Purdy, G.M., Toomey, D.R., Solomon, S.C., 1995. Microearthquake characteristics and crustal velocity structure at 29°N on the Mid-Atlantic Ridge: the architecture of a slow spreading segment. J. Geophys. Res. Solid Earth 100, 24449–24472. https://doi.org/10.1029/95JB02399.

Zhao, Q., Zhao, S., Xu, C., 2022. Hematite exsolutions in corundum from cenozoic basalts in Changle, Shandong Province, China: crystallographic orientation relationships and interface characters. Crystals 12, 905. https://doi.org/10.3390/cryst12070905.